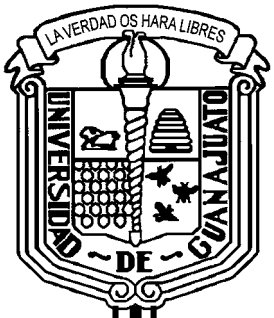



# UNIVERSIDAD DE GUANAJUATO

**Centro de Investigaciones en Optica, A. C.**



# HIGH-ACCURACY PARTICLE POSITIONING TOGETHER WITH OPTIMUM DATA DISPLAY FOR VELOCIMETRY APPLICATIONS


*A dissertation submitted by*

**David Moreno Hernández**


*In partial fulfillment of the requirements for the degree of*

**Doctor in Science (Optics)**

León, Gto. November 2000

# High-accuracy particle positioning together with optimum data display for velocimetry applications

**A dissertation**

**submitted by**

**David Moreno Hernández**

**In partial fulfillment of the requirements for the degree of Doctor in Science (Optics)**

**Centro de Investigaciones en Optica A. C.**

**November 2000**

**Supervisors: Dr. Fernando Mendoza Santoyo**
**Dr. Marcelo Funes Gallanzi (INAOE)**

*To my lovely Isabel*

*To my wonderful sons: Fernando and Daniel*

*To my beautiful daughters: Diana and Sofia*

*To my Father, Mother and Brothers*

*Let not the wise man boast of his*
*wisdom or the strong man boast of his strength or the*
*rich man boast of his riches,*
*but let him who boasts boast about this:*
*that he understands and knows me,*
*that I am the LORD, who exercises*
*kindness, justice and righteousness on earth,*
*for in these I delight," declares the LORD.*

*Jeremiah 9:23,24*

**ACKNOWLEDGEMENTS**

The main acknowledgement is credited to Dr. Fernando Mendoza Santoyo and Dr. Marcelo Funes-Gallanzi for their tireless efforts and guidance associated with this research. The author would also like to thank Dr. Ramón Rodríguez Vera for his generous comments. Thanks are also due to the Consejo Nacional de Ciencia y Tecnología and Consejo de Ciencia y Tecnología del Estado de Guanajuato for my doctoral study grants. Thanks also to the Academic Office, Library and computer center personnel. Finally I would like to thank my very good friends at the CIO such as: Javier Yañez, Marcial Boys, La Rubina, Jesus Cervantes, David Monzon, J. Bujdud, Alma Fuentes, Fede, Don Panchius, Pepe Puga, Ely Taylor, Angeles S. and the famous man called Chon.

## ABSTRACT

# High-accuracy particle positioning together with optimum data display for velocimetry applications

Three-dimensional position and velocity information can be extracted by directly analysing the diffraction patterns of seeding particles in imaging velocimetry using real-time CCD cameras. The Generalised Lorenz-Mie theory is shown to yield quantitative accurate models of particle position, such that it can be deduced from typical experimental particle images with an accuracy of the order of 20 μm and an error of 11 grey levels RMS, data obtained by comparing theoretical and experimental images. Both, the theory and experimental verification of the problem presented here are discussed.

This thesis present also a method which determines the optimum grid size for interpolated velocimetry data, without making any priori assumptions about the velocity fields, the system used or analysis method. The method employs condition number as the main criterion for deciding the adequate grid size for a given data set. Data sets displayed accordingly are directly comparable, independently of differing experimental parameters or data processing methods. The discussion is based on Computational Fluid Dynamics (CFD) data of flow past the near wake of a cylinder from which simulated PIV images were generated. These images were analysed with the proposed method and the velocity estimates compared to the CFD data. The method was also applied to a sample PIV image of turbulent flow in a baffled tube.

# Contents

# LIST OF FIGURES

# NOMENCLATURE

## Chapter 1

| | |
|---|---|
| d | Distance between particles |
| v | Particle velocity |
| t | Time laser pulse |
| *x,y* | Particle coordinates |
| $k_n$ | Noise pedestal |
| σ | Variance of the radialy symmetric Gaussian function |
| $R_{xx}$ | Autocorrelation function |
| *I* | Intensity illumination of particles |
| *r* | Measured position in film plane |
| $r_d$ | Displacement vector |
| $N_S$ | Source density value |
| $N_I$ | Image density value |

## Chapter 2

| | |
|---|---|
| *M* | Magnification |
| $L_k$ | Kolmogorov scale |
| $L_c$ | Characteristic length |
| $L_{pixel\ size}$ | Characteristics pixel size |
| $\nu$ | Viscosity |
| $v_c$ | Characteristic velocity |
| Re | Reynolds number |

| | |
|---|---|
| $N_p$ | Number of pixels |
| $R$ | Sensor resolution |
| $St$ | Stokes number |
| $\rho_p$ | Particle density |
| $d_p$ | Particle diameter |
| $\mathrm{Re_o}$ | Oscillatory Reynolds number |
| $St_o$ | Strouhal number |
| $f$ | Frequency of oscillation |
| $x$ | Center to peak amplitude of oscillation |
| $\rho$ | Fluid density |
| $\mu$ | Absolute viscosity |
| $d$ | Tube diameter |

**Chapter 3**

| | |
|---|---|
| $\lambda$ | Wavelength of the radiation |
| $a$ | Particle diameter |
| $H$ | Magnetic field intensity |
| $E$ | Electric field intensity |
| $k$ | Wave number |
| $\overline{n}$ | Complex refractive index |
| $i$ | The complex number |
| $E^i_{r,\theta,\varphi}$ | Incident Electric field intensity in spherical coordinates |
| $E^s_{r,\theta,\varphi}$ | Scattered Electric field intensity in spherical coordinates |

| | |
|---|---|
| $S_{1,2}$ | Mie amplitude functions |
| $\pi_n^m, \tau_n^m$ | Legendre functions |
| $a_n, b_n$ | Mie coefficients |
| $\psi_n, \chi_n, \xi_n$ | Riccati-Bessel functions |
| $P_n^m$ | Legendre polynomials |
| $\tilde{r}$ | Normalized distance from particle to the scattered light observation point |
| $r$ | Distance from particle to the scattered light observation point |
| $i_1$ | Perpendicular light scattered intensity |
| $i_2$ | Parallel light scattered intensity |
| $a_r$ | Particle radio |
| $\alpha$ | Size parameter |
| $U_{TM,TE}$ | Bromwich scalar potentials |
| $g_{TE,TM}$ | Coefficients characterizing the incident profile. |
| $\omega_{0x}$ | X directions beam waist |
| $\omega_{0y}$ | Y directions beam waist |
| ~ | Means normalization to particle radius |
| $(r, \theta, \varphi)$ | Spherical coordinates system |

**Chapter 4**

| | |
|---|---|
| $d_e$ | Image diameter |
| $d_s$ | Point response function diameter |
| $d_p$ | Particle diameter |
| $\lambda$ | wavelength |

| | |
|---|---|
| $M$ | Amplification |
| $f/\#$ | F/number |
| $f$ | Focal length |
| $E$ | Electric field |
| $\Delta_o$ | Thickness of the lens |
| $n$ | Refractive index of the lens |
| $r_m$ | Lens radius |
| $z_m$ | Axis location |
| $k$ | Wave number |
| $J_o$ | Bessel function of the first kind |
| $Y$ | Intensity at the image plane |
| $a_r$ | Particle radius |
| $\sim$ | Means normalization to particle radius |

## ABBREVIATIONS

| | |
|---|---|
| LDV | Laser Doppler Velocimetry |
| LDA | Laser Doppler Anemometry |
| L2F | Laser Two Focus |
| LIF | Laser Induced Fluorescence |
| PIV | Particle Image Velocimetry |
| DGV | Doppler Global Velocimetry |
| PTV | Particle Tracking Velocimetry |

| | |
|---|---|
| 3D PIV | Three Dimensional Particle Image Velocimetry |
| CCD | Charge-Coupled Device |
| GLMT | Generalized-Lorenz Mie Theory |
| LMT | Lorenz Mie Theory |
| BSP | Bromwich Scalar Potentials |
| TE | Transverse Electric |
| TM | Transverse Magnetic |
| CFD | Computational Fluid Dynamics |
| DNS | Direct Numerical Simulation |
| LSV | Laser Speckle Velocimetry |
| SLS | Scattered Light Speckle |
| HPIV | Holographic PIV |
| TV | Tunneling Velocimetry |
| RMS | Root Mean Square |
| SVD | Singular Value Decomposition |
| TSVD | Truncated Singular Value Decomposition |
| AIP-PIV | Analysis Integrated Processing PIV |

# LIST OF PUBLICATIONS, CONFERENCES AND WORK IN PREPARATION DERIVED OF THIS RESEARCH

## Publications

1. D. Moreno, F. Mendoza Santoyo, M. Funes-Gallanzi and S. Fernandez, “An optimum velocimetry data display method”, Optics and Laser and Technology, **32** , pp. 121-128 (2000).

2. D. Moreno, F. Mendoza Santoyo, J. Ascención. Guerrero, M. Funes-Gallanzi, "Particle positioning from CCD images using Generalized Lorenz-Mie Theory and comparison to experiment", Applied Optics, **39**(28), pp. 5117-5124 (2000).

3. J. A. Guerrero, F. Mendoza Santoyo, D. Moreno, M. Funes-Gallanzi, S. Fernandez-Orozco, "Particle positioning from CCD images: experiments and comparison to the Generalized Lorenz-Mie Theory", Measurement Science and Technology, **11**(5), pp. 568-575 (2000).

## Papers submitted

J. A. Guerrero, F. Mendoza Santoyo, M. Funes-Gallanzi, D. Moreno and P. Padilla Sosa, "Tunneling Velocimetry: A technique combining 3D velocimetry with Parameter Sensitive Paint". submitted to Review of Scientific Instruments, 2000.

## Paper in preparation

D. Moreno, F. Mendoza Santoyo, J. Ascención. Guerrero and M. Funes-Gallanzi, “The case of a spherical wave-front in the Generalized Lorenz-Mie Theory including a comparison to experimental data”, to be sent to Optics Letters.

## Conference Presentations

1. D. Moreno, F. Mendoza Santoyo, M. Funes Gallanzi, "obtencion y desplegado de datos experimentales en PIV (Velocimetría de partículas por imágenes)", presentado en el XL Congreso Nacional de Física, organizado por la Sociedad Mexicana de Física, Monterrey, N.L., México, octubre de 1997.

2. D. Moreno, F. Mendoza Santoyo, M. Funes Gallanzi, "Posicionamiento de una partícula en tres dimensiones utilizando una sola camara", presentado en el XLI Congreso Nacional de Física, organizado por la Sociedad Mexicana de Física, San Luis Potosí, S.L.P., México, octubre de 1998.

3. D. Moreno, F. Mendoza Santoyo, J. Ascención Guerrero, y M. Funes-Gallanzi, "Modelo teórico de la imagen de una partícula esférica iluminada con una hoja de luz, para aplicarse a PIV: teoría y comparación con el experimento", presentado en el XLII

congreso Nacional de Física, organizado por la Sociedad Mexicana de Física, Villahermosa, Tabasco, México, noviembre de 1999.

4. J. A. Guerrero, F. Mendoza-Santoyo, D. Moreno y M. Funes-Gallanzi, "Analisis experimental de imágenes de PIV para determinar la velocidad fuera de plano de un fluido", Congreso Nacional de Física, organizado por la Sociedad Mexicana de Física, Villahermosa, Tabasco, México, noviembre de 1999.

# Introduction

Optical techniques are widely used in fluid mechanics to observe and measure properties of flow fields such as pressure, temperature, density and velocity. Many of these techniques are qualitative, but of great value since they provide guiding intuition for further research by quantitative means. Optical techniques are well known for their wide nonintrusive properties as compared with methods like the pitot tube or the hot-wire techniques. In the last few years a lot of successful development effort has been oriented towards measuring the velocity.

In 1964 Yeh and Cummins [1] first described the use of a laser to measure the velocity of a liquid flow and, thus beginning a revolution in using non-intrusive techniques to make detailed diagnostic measurements within a flow field. Light scattered from small particles in the laser beam path, was collected by a lens system and directed collinearly with the laser beam, called the reference beam, to the photocathode surface of a photomultiplier. Since the photocathode surface follows a square law detector, the optical frequency of the reference beam and the Doppler shifted optical frequency from the scattered light are mixed together (heterodyne effect) yielding a signal containing the difference (Doppler) frequency between the two light waves. Using the relations from the Doppler effect, the particle velocity is linearly related to the wavelength of the laser light, the sine of the half angle between the laser beam and the collected scattered light, and the resulting difference (Doppler) frequency.

This first system for measuring velocity gave way to a wide range of flow field velocity measurement techniques that are currently available for aerodynamic and turbomachinery research, amongst other fields. Laser Doppler Anemometers (LDA's), Laser Two Focus (L2F), Laser Induced Fluorescence (LIF), Particle Image Velocimetry (PIV), Doppler Global Velocimetry (DGV), are perhaps the most commonly applied optical velocimetry methods in wind tunnel and flight test applications. Each of these techniques offer unique advantages for a particular need or test environment. Unfortunately, each of these methods also share common weaknesses.

Laser Doppler Anemometers and Laser Two Focus are all point measurement techniques. Physical movement, or traversing, of the probe/measuring volume is required to identify multi-component velocity data over a large flow area. Data acquisition is, as a result, typically time consuming and simultaneous identification of global velocity data is essentially impossible. These techniques are effective for steady flows, though there has been a shift towards developing Laser Doppler Velocimetry (LDV) to deal with unsteady flows

In most cases, global simultaneous data acquisition is preferred like Particle Image Velocimetry (PIV), Laser Induced Fluorescence (LIF) and Doppler Global Velocimetry (DGV). These can improve testing time, costs, and provide the ability to resolve unsteady flow features.

Laser Induced Fluorescence is an attractive technique to measure pressure/temperature. There are different implementations of this technique but the most popular has been that based on an argon-ion laser with iodine as a seed [2]. The argon laser excites iodine molecules that are not in the ground state. However, to calculate physical parameters from the measured LIF signal, the optical set-up and laser tuning become rather complicated and difficult to apply for practical flows. Measurements of temperature at a fixed narrow pressure range have been reported [3]. Pressure and velocity measurements, based on the Doppler shift of the fluorescence spectral lines, at a set narrow range of temperatures [4] have also been reported. The main problem with LIF is its cross dependence of the fluorescence on pressure and temperature.

DGV makes velocity measurements from the frequency shift of light scattered by particles in the flow. Velocity is measured by means of a frequency-to-intensity converter, typically an iodine-vapour absorption cell [5]. The direction of the velocity component measured is determined by the direction of the light sheet and the direction of observation. DGV offers a number of advantages not found in other planar measurement techniques. Unlike particle image velocimetry (PIV) and particle tracking velocimetry (PTV), there is neither a need to resolve discrete particles nor their displacement over a short time interval. DGV requires to record the light scattered by the illuminated particles, inherently allowing the size of the field of view to be chosen arbitrarily. Image resolution is not vital for DGV, which makes the technique attractive in situations with poor optical access or in media with varying refractive index, such as internal flows or combusting media.

PIV is a whole-field method used for measuring fluid velocity almost

instantaneously [6,7]. This approach combines the accuracy of single-point methods with the multi-point nature of flow visualisation techniques. A pulsed laser source is a thin light-sheet and a double exposure of the light scattered by particles, introduced to the flow as seeding, is recorded by a camera during a short sampling period. The viewing position lies orthogonal to the plane of the light sheet. The recording contains image pairs of a particle, their displacement encoding the velocity field. An analysis system is employed to measure velocity from the displacement information, with previous knowledge of the time separation between pulses.

Conventional Particle Image Velocimetry (PIV), for instance, suffers from an intrinsic limitation because it yields 2D data, hence neglecting the third velocity component. For this reason, techniques for 3D PIV have recently evolved as an area of intensive research [8-22], with some success at the cost of increasing complexity. The increased complexity and the limited optical access found in industrial applications, means that many of these techniques, though of academic interest, cannot be used in practical industrial applications. Shortly, these techniques involve scanning light-sheets, stereoscopic views, holographic recording, parallel light-sheets, graded intensity light-sheets, or mixtures thereof.

For practical applications, restricted viewing eliminates stereoscopic approaches. Robustness and ease to perform an experiment make holography an unattractive option due to the fact that it involves a lengthy developing process and therefore is slow to yield results, although its large depth of field and storing capacity makes it somewhat attractive. Scanning light-sheets are difficult to operate with restricted optical access and high speeds, so they have not been employed in industrial environments. Moreover, practical application

errors reported for all these techniques are in general unacceptably large.

The use of CCD cameras have shown their worth in industrial applications, and are in increasingly widespread use as an image recording medium. Restricted optical access to flows of interest, such as those found in turbomachinery, mean that only one camera is often what can be accommodated. An extension of the high-accuracy technique [23] to three dimensions exploiting the digital representation of particle images, in intensity as well as spatially, has been developed [24]. In this work, due consideration is given to the need for 3D particle positioning at low magnification, such that an adequate investigation region may be interrogated. For a pattern-matching low-magnification approach to work, detailed models of the behaviour of particles illuminated by monochromatic light must be derived. An accurate model of the particle image preferably relies on the Generalised Lorenz-Mie Theory [25] (GLMT) which is applicable to plane, Gaussian or elliptically (light sheet) shaped incident beams.

In an attempt to solve some of the above cited problems this thesis proposes the use of the GLMT for particle image calculation. It is a novel contribution to three dimensional velocity measurements in these fields. Intensity and spatial information of a particle image diffraction pattern is used to calculate its three-dimensional position, and hence velocity information using real-time CCD cameras. The model uses a GLMT to calculate the external electromagnetic field resulting from the interaction of a known shaped beam with a finite absorbing spherical particle. Propagation of the electric field through the imaging system components is developed from scalar viewpoints using a thin lens transformation and the Fresnel approximation to the Huygens-Fresnel propagation equation. The

theoretical model is also useful in other application areas such as particle-sizing, as well as in examining, for instance, the effect of changing aperture size, the nature of image variation with the degree of particle defocus and the parameters adjustment required for CCD cameras.

Another important task in PIV is the ability of provide velocity data, obtained simultaneously, on a distributed spatial grid. This is of interest when using the data to validate CFD (Compute Fluids Dynamics) codes. Moreover, it is important to know how much detail can be obtained by sparse random 2D point measurements of a velocity field. This thesis also includes a method to determine the optimum grid size for interpolated velocimetry data, without making any a-priori assumptions about the velocity fields, the system used or analysis method. The method employs condition number as the main criterion for deciding the adequate grid size for a given data set. Data sets are directly comparable, independently of differing experimental parameters or data processing methods. This method illustrates the advantage of using velocimetry for unsteady flow research, i.e., by using a comparatively small number of measurement points a detailed mesh of the underlying flow field can be derived. Thus, although this velocimetry methods delivers a limited number of measurement points, as compared to DGV, for instance, which essentially yields a measurement per pixel, in general a high measurement data rate is not required to adequately reconstruct a flow field.

The thesis was ordered such that the reader can understand the PIV technique and how Three Dimensional PIV has evolved in the last years. After that, a theoretical basis is

given to improve the early particle image model to obtain, with high accuracy, in-plane and out-of-plane particle position.

Chapter 1 presents a study of PIV and 3D PIV. This chapter discusses important subjects such as methods of image analysis in PIV, for high and low image density seeding particles. Low image density seeding particles is important in this thesis because it is possible to extract three dimensional position and velocity information from particle images. Furthermore, the model presented in this thesis can also improve the in plane position of particle image.

In chapter 2 a method is proposed to determine the optimum grid size for interpolated velocimetry data, without making any apriori assumptions about the velocity fields, the system used or analysis method. The method employs condition number as the main criterion for deciding the adequate grid size for a given data set. Data sets displayed are directly comparable, independently of differing experimental parameters or data proccesing methods. The discussion is based on computational fluid dynamics (CFD) data of flow past near the weak of a cylinder from which simulated PIV images were generated. These images were analysed with the proposed method and the estimates velocity is compared with the CFD data. The method was also applied to a sample PIV image of turbulent flow in a baffled tube.

Chapter 3 discusses light scattering by spherical particles. It starts with a study of classical Lorez-Mie theory (LMT) proposed for wave plane illumination. The Generalized Lorenz Mie Theory (GLMT) is treated giving the case of beam shaped illumination of the

particle. The light scattering diagram is shown for different particle sizes and different beam shaped illumination.

The scattered light by a particle is collected by a lens and propagated to the image plane. Chapter 4 discusses the propagation of the electric field scattered by the spherical particle using the thin-lens transformation and the Fresnel approximation to the Huygens-Fresnel propagation equation. The model also includes Seidel aberrations of the optical system used.

Chapter 5 discusses results obtained by using the theory put forward in chapters 3 and 4. Diagrams of particle image are shown as simulation for different parameters and the experimental results show a good agreement with the model explained in this thesis. The particle image diagrams show that the model does improve the in plane particle position, and the spatial information is used to determine the out of plane position. Finally, chapter 6 gives the general conclusions and future work.

**References**

1. Y. Yeh and H. Z. Cummins, “Localized Fluid Flow Measurements with an He-Ne Laser Spectrometer”, Applied Physics Letters, **4**, pp. 176-178 (1964).

2. J. C. McDaniel, "Investigation of Laser-Induced Iodine Fluorescence for the Measurement of Density in Compressible Flows", Stanford University, SUDAAR No. 532, 1982.

3. M. Inoue, M. Masuda, M. Furukawa and T. Muraishi, "Diagnosis of Three Dimensional Transonic Flow Fields with Laser-Induced Iodine Fluorescence", ASME FED, **218**, pp. 163-170 (1995).

4. F. Lemoine, X. Lefevre and B. Leporq, "Pressure and Velocity Measurements in Compressible Flows Using Iodine Fluorescence Induced by a Single-Mode Laser", ASME FED, **218**, pp. 81-87 (1995).

5. H. Komine, “System for measuring velocity field of fluid flow utilizing a laser Doppler spectral image converter”, US Patent 4 919 536 (199)

6. T. D. Dudderar and P. G. Simpkins, "The development of scattered light Speckle Metrology", Nature, London, **270**, pp. 45-47 (1977).

7. M. Raffel, C. Willert and J. Kompenhans, "Particle Image Velocimetry", Springer-Verlag, (1998).

8. V. Gauthier and M. L. Riethmuller, "Application of PIDV to complex flows: Measurements of third component", Von Karman Institute Lectures, Series 6, Rhode Saint Genese, Belgium, (1988)

9. J. Westerweel and F. T. M. Nieuwstadt, "Performance tests on 3-dimensional velocity measurements with a two-camera digital particle image velocimeter", ASME Laser Anemometry, **1**, pp. 349-355, (1991)

10. C. Gray, C. A. Greated, D. R. McCluskey and W. J. Easson, "An analysis of the scanning beam PIV illumination system", Measurement Science Technology, **2**, pp. 717-724, (1991)

11. H. Meng and F. Hussain, "Holographic particle velocimetry: a 3D measurement technique for vortex interactions, coherent structures and turbulence", Fluid Dynamics Research, **8**, pp. 33-52, (1991)

12. C. Brucker, "Study of vortex breakdown by particle tracking velocimetry", Experiments in Fluids, **13**, pp. 339-349, (1992).

13. P. J. Bryanston-Cross, M. Funes-Gallanzi, T. R. Quan and T. R. Judge, "Holographic particle image velocimetry (HPIV)", Optics and Laser Technology, **24**, pp. 251-256, (1992).

14. F. Dinkelaker, M. Schaffer, W. Ketterle and J. Wolfrum, "Determination of the third velocity component with PTA using an intensity graded light sheet", Experiments in Fluids, **13**, pp. 357-359, (1992).

15. C. E. Willert and M. Gharib, "Three-dimensional particle imaging with a single camera", Experiments in Fluids, **12**, pp. 353-358, (1992).

16. B. Ovryn and E. A. Hovenac, "Coherent forward scattering particle image velocimetry: application of Poisson's spot for velocity measurements in fluids," in Proceedings, Optical Diagnostics in Fluid and Thermal Flow, S. S. Cha and J. D. Trolinger, Eds. SPIE **2005**, pp.338-348, (1993).

17. A. K. Prasad and R. J. Adrian, "Stereoscopic particle image velocimetry applied to liquid flows", Experiments in Fluids, **15**, pp. 49-60, (1993).

18. R. J. Adrian, C. D. Meinhart, D. H. Barnhart and G. C. Papen, "An HPIV system for turbulence research", ASME Holographic Particle Image Velocimetry, **148**, pp.17-21, (1993).

19. Y. G. Guezennec, Y. Zhao and T. J. Gieseke, "High-speed 3D scanning particle image velocimetry (3-D PIV) technique", Proceedings of The Seventh International Symposium on Applications of Laser Techniques to Fluid Mechanics, LADOAN-Instituto Superior Tecnologico, Lisbon, Portugal, 26.2.1-26.2.10, (1994).

20. A. K. Prasad and K. Jensen, "Schiempflug stereocamera for particle image velocimetry in liquid flows", Applied Optics, **34**, pp. 7092- 7099, (1995).

21. K. D. Hinsch, "Three-dimensional particle velocimetry", Measurement Science and Technology, **6**, pp. 742-753, (1995).

22. A. Lecerf, B. Renou, D. Allano, A. Boukhalfa, and M. Trinité, "Stereoscopic PIV: validation and application to an isotropic turbulent flow", Experiments in Fluids, **26**, pp. 107-115, (1999).

23. M. Funes-Gallanzi, "High Accuracy Measurement of Unsteady flows using digital PIV", Laser & Optics Technology, **30**, pp. 349-359, (1998).

24. P. Padilla Sosa and M. Funes-Gallanzi, "High Accuracy at Low Magnification 3D PIV Measurement Using the Concept of Locaels", submitted to Optics and Laser Technology, (2000).

25. G. Gouesbet and G. Gréhan, “Sur la généralisation de la théorie de Lorentz-Mie”, Journal Optics (Paris), **13**, pp. 97-103, (1982).

# Chapter 1

# Introduction to Particle image velocimetry (PIV) and Three dimensional PIV

## 1.1 Introduction

This chapter discusses Particle Image Velocimetry in detail. PIV is an optical, whole filed measurement technique that uses the light scattered by (seeding in flow) particles to estimate the velocity of the flow. The main advantages are that it is non-intrusive, it acquires data rapidly, and it display an instantaneous whole field visualisation of the flow field.

A comprehensive introduction to PIV is contained in the paper by R .J. Adrian [1] and in the book written by M. Raffel et al. [see reference 7 in introduction]. Particle image displacement velocimetry (PIV) is described as a method of measuring fluid velocity almost instantaneously, over extended regions of a flow domain. The method combines the accuracy of single-point methods, such as Laser Doppler Velocimetry, with the multi point nature of flow visualisation techniques. Numerous research groups have worked along these lines during the past decade. PIV is one of several approaches that has been aimed at measuring accurately whole-field velocity in two or three dimensions.

## 1.2 History of Particle Image Velocimetry

The development of particle image velocimetry can be traced back by studying the different names this technique has been given over its short history. Because early measurements produced speckled images instead of single resolved particle images, the technique was assigned the term scattered light speckle (SLS) metrology, and the photographic records were called specklegrams. Generally the term speckle velocimetry was used for metrology, employing for evaluation the Young's fringes that the double exposure speckle photographs yield. Their twin structure is difficult to identify in the photograph, so their diffraction pattern (Young's fringes systems) is studied to obtain particle displacement information. The fringe orientation is perpendicular to the direction of displacement, and the fringe spacing is inversely proportional to the magnitude of the displacement. This interrogation scheme was adopted in flow velocimetry. Gradually it was realized that speckles are not necessary for flow diagnostics. If particle images do not overlap (which depends on seeding density and imaging system aperture), discrete image pairs are produced, and the records become multiple-exposure photographs that can be produced even with classical illumination [2]. There are good reasons to prefer this mode of recording because the speckle mode is more sensitive to decorrelation by out-of plane particle motion. New names were added, laser speckle velocimetry (LSV) or photography (LSP), with the interrogation technique identical to that used in speckle metrology. But researchers in the field became more precise in their terminology, and today the term Particle Image Velocimetry (PIV) is widely accepted [3,4], always referring to the same principle of data evaluation and method to study flow fields.

High image density particle image velocimery was established as a distinct mode of pulsed light velocimetry by Pickering and Halliwell [5], and Adrian [3], who argued that

the concentrations of scattering particles that are practical in experimental fluid mechanics are often not dense enough to create speckle patterns. Thus, unless one makes extreme efforts to seed the flow with high concentrations of carefully chosen paaticles, high image density PIV is better than LSV. Many experiments that had been labeled LSV were indeed PIV, as Meynart [6] seems to have recognized. Further studies of the scattering properties of particles in relation to photographic imaging (Adrian and Yao [7] ) indicated that individual particles in the 1-10 μm range would produce more detectable images at lower mass loadings than the large numbers of fine particles that would be needed to produce speckle.

### 1.3 Particle Image Velocimetry: The method

A double exposure of the light scattered by particles in the flow, when they are lit by a pulsed light source, is recorded during a sampling period, so the image records particle pairs. The displacement between the particle pair images and the time of the sampling period related to flow velocity (figure 1.1).

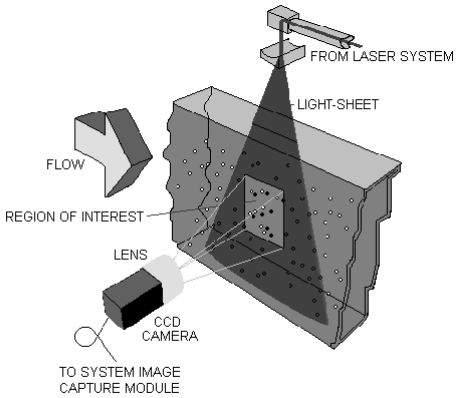


**Figure 1.1 Classical PIV setup**

The density of the particles has to be matched to the finest flow details, and the time between exposures has to be adjusted to ensure that particle pair separation is small compared to this structures scale. On the other hand, however, the displacement must be large enough to be measured accurately. Furthermore, the accuracy in position measurement depends on the size of the imaged particles. These should be small, and the exposure time should guarantee an unblurred image.

The seeding marker used to visualise flows in PIV is a small particle, such as Styrene, or liquid droplet (such as water) in a gaseous flow. Choosing the proper seeding particle for PIV applications is a classic case of compromise. A smaller particle will more faithfully follow the fluid flow, increasing displacement measurement accuracy. A larger particle will scatter more light, increasing signal strength resulting in better position measurement. The chosen particle size is often determined by the ability of the optical system to see that particle, and accepted aerodynamic inaccuracies. The sensitivity of the imaging system is in turn constrained optically and financially.

A high power illumination source is required because the particles being imaged are so small. Steady light sources such as ordinary lamps or cw lasers can be strubled or modulated to form pulses, but this often wastes considerable amounts of energy. It is more efficient to use pulsed sources such as flash lamp, spark discharges, or pulsed lasers. Xenon flash lamps can emit several hundred joules in pulses as short as 1 μs, but only a small fraction of this energy can be used to form a thin light sheet. Pulsed lasers such as Nd:YAG produce high energies (around 300 mJ/pulse) in pulses of very short duration, of the order of 10 to 25 ns, being appropriate for PIV applications.

The choice of the recording medium is made on the basis of the size of flow field to be recorded and the required image resolution. The principal difference between film and video is spatial resolution. A CCD camera offers about 512x512 pixels, but high-resolution arrays are available with up to 3072x2048 pixels, but they are expensive and relatively slow. Films, on the other hand, offer much higher resolution. A standard 35-mm film frame of 300 lines per millimeter, Kodak Technical Pan for example, contains 10,500x7500 pixels, and a 100 mm x 125 mm frame of portrait format contains 30,000x37500 pixels. We shall see that this additional resolution leads to approximately 10 times better spatial resolution and 10 times better accuracy, as compared to a standard video camera. Film tends to be used for high resolution and wide dynamic velocity range measurements of fluids, whereas video recording is suitable for lower resolution, lower accuracy flow measurements, for higher accuracy measurements over smaller fields of view, for measurements of larger particles in two-phase flow, and obviously CCD's show real time images of the particle in the flow.

### 1.4 Methods of image analysis in PIV

PIV consists of two steps: the recording of a suitably illuminated configuration of small particles within the flow, usually as a double, rarely a multiple-exposure record, traditionally on a single photographic frame, and the analysis of this record to obtain the particle pair spatial distribution and then the velocity. A lot of time has to be employed in the processing of such PIV records, devising schemes to extract the desired displacement information from them and in optimizing the signal-to-noise ratio. To understand more about these techniques and their limitations, we will look at a theoretical analysis of data stored in the double exposure.

According to Adrian [1] the seeding density is quantified by the source density value $N_S$. If $N_S>>1$, the seeding density is large and many particles occupy a characteristic volume, the resolution cell. In these circumstances, interference of the scattered light from these particles will take place in the image plane of the camera and a speckle pattern will be formed. If $N_S<<1$, the seeding density is small and implies fewer images. In order to quantify this feature, the image density $N_I$, the number of particle images found in an interrogation cell, is used. High image density corresponds to $N_I>>1$, while $N_I<<1$ correspond to low image density, both cases are shown in figure 1.2. In the latter PIV mode, the abundance of images makes the tracking of individual particles time consuming, measuring the displacement of small groups of images, as we will see in next section.

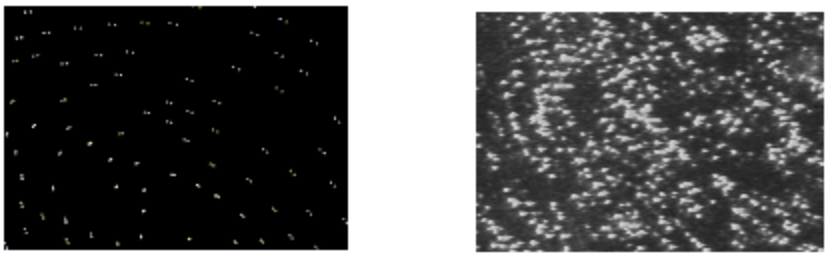

a) b)

Figure 1.2. PIV images, (a) low image density, (b) High image density

### 1.4.1 Low image density

Low image density PIV studies, interrogate flow images theta have low concentration of particle images to allow individual trajectories to be followed. The analysis of images in this regime often begins with digital preprocessing. A statistical procedure is used to quantify the gray level images distribution, followed, where appropriate, with contrast stretching, thresholding, and edge detection, possibly with the

binarization of the images. The resulting particle images are reduced to single pixel size, located at the weighted image centers. Specific statistical analysis then groups the particle images and quantifies the local displacements. This approach is illustrated in Adamczyk and Rimai [8], Agui and Jimenez [9], and Grant and Liu [10].

It is known that seeding-particle concentrations in high speed flows are low and so do not justify the use of correlation-based techniques. The spatial pairing strategy allows the original image and the vector results to be overlaid, which aids in the interpretation of the flow structure. So, the intuitively simplest processing method, for resolved particles, is the direct analysis of the PIV recording to determine the distance and direction through which the particles have moved to between exposures. The problem then is to identify a particle and its partner. In densely seeded flows the probability of mis-matching particle images is high. One method that helps to resolve this problem is to pulse the laser several times, to create multiple images of each particle, which provides additional criteria for allocating particles to unique groups. Also, two pulses can be used, each pulse of a different color, such that it is possible to distinguish the first and second partner in the pair, thereby accounting for any directional uncertainty.

Solving PIV images involves mainly two steps. Firstly, the pre-processing stage is used for improving the image quality and extracting the relevant information about the location of particles in the field. Combined methods of signal to noise enhancement (e.g. binarisation by thresholding, contrast enhancement, noise filtering), and calculation of particle image centre (e.g. edge detection, centre of mass) are involved. Secondly, the main processing stage includes algorithms for reconstructing particle trajectories, such as pairing tracking, and performing image correlation and peak extraction, followed by the calculation of the velocity vectors and the generation and representation of coherent velocity maps.

One of the major problems, yet to be solved with exactitude, when processing PIV data is the accurate positioning of the centre of the particle image. Several methods have been proposed to particle image centre estimation, in the following we will explain some of them.

**Highest intensity pixel**. This approach consists in finding the pixel with the highest intensity value, also called the zero moment. It also corresponds to the maximum of the gaussian function and the centre of the particle if no distortion or large noise is present in the data. In this case no previous operation performed on the image is necessary but the errors are as high as 1 pixel in x direction and 1 pixel in y direction for each particle, which gives an overall error of 2.82 pixels for the distance between particles (figure 1.3).

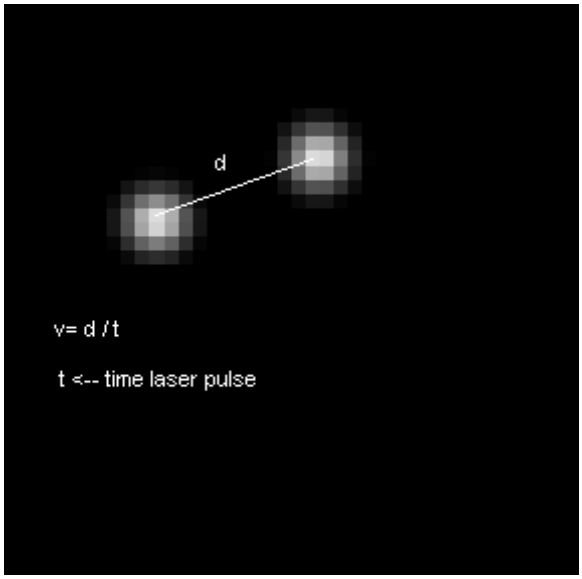


Figure 1.3 Velocity calculation by the highest intensity pixel method.

**Centre of the bounding box**. The method involves a thresholding step and black and white edge detection operation prior to the construction of the bounding box. The centre of the particle becomes the intersection of the diagonal of the bounding box. This implies that, for obtaining consistent results, the intensity profile needs to be nearly symmetric. In this case, the individual error is reduced to 0.5 pixels and the overall error becomes 1.41 pixels.

**Bidimensional gaussian fit**. Assuming a gaussian geometrical image for a spherical particle, and a constant intensity of the illuminating beam on the sphere surface over the time interval of a pulse, the intensity distribution of the focused image is expected to be well approximated by a symmetric, bidimensional gaussian.

$$I(x,y) = A \cdot \exp\left\{ - \frac{\left[ (x - x_0)^2 + (y - y_0)^2 \right]}{\left( 2 \cdot \sigma^2 \right)} \right\} + k_n$$

Where A is the amplitude and $\sigma$ is the variance of the radially symmetric gaussian, and the centre has coordinates $(x_0,y_0)$, $k_n$ is the noise pedestal. Starting from these theoretical premises and using initial guesses for the parameters xo, yo and $\sigma$, the algorithm uses the Nealder-Meade bidimensional fitting method for the particle data. The process is iterative. The initial values of the parameters do not influence the final results, but a more accurate guess diminishes the convergence time of the algorithm.

**Autocorrelation.** The Autocorrelation or individual correlation method, is a Fourier based method also used for low seeding density PIV images. It involves two initial steps from

which a subset of the image, containing a particle pair, or track, can be extracted. Firstly, a low resolution algorithm for particle identification, such as the highest intensity pixel or the centre of the bounding box, determines the interrogation cell and secondly, a tracking method for particle grouping determines the area over which the local correlation is performed. The dc component and the first peak of the resulting power spectrum correspond to the image transformation from the correlation cell with itself and with the pair image respectively. In this case, its not the individual positioning of the particles but the separation distances the ones that are evaluated directly by measuring the distance between the peaks, (figure 1.4).

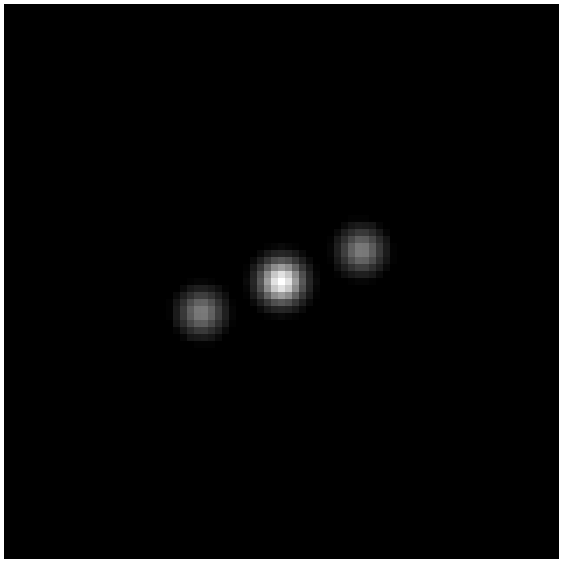

Figure 1.4 Velocity calculation by autocorrelation method.

**Locales concept**. Funes-Gallanzi [11] used the concept of locales for position estimation to achieve the objective of high accuracy PIV measurements. This approach makes use of the

fact that by considering the possible digital representations of the Gaussian particle profile, regions of indistinguishable positions can be derived. These positions are referred to as "locales". By considering the density, distribution, and shape of these locales, the precision can be estimated and an accurate (no worse than 0.5% error for a typical PIV image) in-plane velocity field can be obtained. The concept of locales can also be applied to find correlation peaks by a simple extension of the concept.

### 1.4.2 High image density

High image density PIV uses particle concentrations large enough to ensure that every interrogations cell contains many images. The main features of high image density PIV are that almost every interrogation cell contains enough particles to yield a measurement, and that the large number of images makes it difficult to track individual particles. The methods of interrogation that are currently in use are primarily statistical approaches that probabilistically infer the proper pairings and measure the average displacement of the group of particles in the interrogation cell.

**Young's fringe method**. The Young's fringe method of analysis was extensively used in the early days to analyze high image density PIV images recorded in photographic film. A laser beam illuminates the film of the flow. The transparency and the plane in which the diffraction pattern is located can be observed at the principal focal planes of a converging lens. The fringe pattern is then Fourier transformed in order to obtain of the phase and the amplitude of the transmitted light, coming from the interrogation region [12]. The fringe

spacing and fringe direction are used to calculate the amplitude and direction of the particle image displacement.

**Autocorrelation**. Fourier transformation of the fringe pattern yields the spatial autocorrelation function,

$$R_{xx}(r_d) = \int I(r)I(r+r_d)dr$$

of the light intensity $I$, transmitted through the interrogation area of the flow image transparency $r$ is the measured position in the film plane and $r_d$ is the displacement vector. The autocorelation contains noise due to film grain effects, electronic noise, and spurious particle pairing. The autocorrelation function has a zero-order peak at the origin with two first-order peaks at displacements of plus-and-minus the displacement between particle images. Peaks also occur due to random correlation between particle images. The ratio of the second tallest peak to the tallest peak is used to validate peak selection by acting as a variable threshold operator. The velocity is estimated from the distance between the centroids of the zero-order and first-order peaks, and is an average of the velocity in the interrogation volume [13].

**Crosscorrelation**. Crosscorrelation can be used [14] in analyzing single-frame, double or multiple-exposure PIV images. In single frame analysis the correlation is performed between a first and a second window whose position is chosen from a local estimate of the mean velocity obtained, for instance, by an autocorrelation procedure. The second window

is larger than the first, so the probability of unpaired images is reduced and the signal-to-noise ratio increased [15].

### 1.5 Three dimensional Particle image Velocimetry (3D PIV)

Classical PIV suffers from several major disadvantages. For instance, the technique of dual-point optical access needed for orthogonal viewing of a thin light sheet is intrinsically 2D, seeding side-scattering efficiency is very low, and it cannot cope with arbitrary velocity magnitudes. Alternative techniques for PIV three-dimensional investigation of fluid flows have been proposed, at the cost of increased complexity and optical access, and in some cases giving up a real-time measurement capability.

Experimental and processing difficulties associated with the extension of PIV to three-component velocity measurements have so far hindered the acceptance of any universal scheme. Most approaches are multiple/moving light sheets [16], holographic [17], or stereographic [18] with some studies combining these techniques [19].

#### 1.5.1 Stereo PIV.

StereoPIV is the natural way formed for PIV. StereoPIV is the determination of the flow velocity in all 3 dimensions rather than two, as was the case in traditional PIV. To obtain the 3rd component of velocity, it is necessary to use two cameras or use cunning optical effects. Many StereoPIV systems have been proposed, the following being the most interesting ones.

Multi-camera systems, such as the work of Delgado et al. [20]. This work describes one of the earliest attempts at StereoPIV. It uses Laser Speckle Velocimetry, a form of PIV that uses a very high seeding density. This is advantageous as it provides far more

information of the flow than flows with a smaller seeding density. That paper describes two techniques of StereoPIV using two cameras; one where two cameras are parallel to one another (translation method), and the other where the cameras are not parallel to one-another (angular displacement method). The paper also show that these methods had potential. He also highlights the pros and cons of the two types of methods.

Single-camera systems, such as the work of Bryanston-Cross [21]. This was an idea proposed at the Optical Engineering Laboratory (University of Warwick) that uses the phenomena of diffraction, and the diffraction rings produced, to calculate the depth of an object. The size of the diffraction rings is proportional to the depth of the particle in the flow. Thus an image of a fluid flow will contain information on the position of the particle in all 3 dimensions ('x' and 'y' information is given by the position of the particle on the image, and the 'z' information is given by the size of the diffraction ring). The theory is based on a paper by Ovryn and Hovenac [see reference 16 in Introduction]. The paper shows that at initial stages, this method gives an accuracy of 10% on the speed of the particle in the out of plane component. However, much more development needs to be carried out on this method.

Ushijihama et al [22]. This system differs from other StereoPIV systems in that it uses two light sheets perpendicular to one another rather than just one as with most other StereoPIV systems. It uses a mathematical model based on variational analysis in order to extract all the components of velocity. Other 3-D StereoPIV methods include the use of holograms to obtain the out of plane component. One such paper describing its uses is by Skarman et al [23].

### 1.5.2 Holographic PIV

Holographic PIV (HPIV) measures three components of velocity in a volume of flow. Multiple reference beam holography methods enable recording of different planes in the flow. HPIV has used both in-line (Gabor) holography and off-axis (Leith-Upatnieks) holography. Holographic film has a much higher resolution than that usually used in PIV. It also needs more light on it in order to record the particle consequently more scattered light is required to obtain a satisfactory image.

Off axis holography is easily disturbed by vibration, noise, or inaccurate reproduction of the reference beam during reconstruction. Consequently, the in line method, using forward scattering, has been favored in many studies. A single laser beam passes through the seeded flow region. The unscattered light is called the reference beam, while light scattered from seeding particles comprises the object beam. The interference of these two beams is recorded on a holographic plate. Three-dimensional information is obtained from the reconstructed image by using optical systems, with a shallow depth-of-field, along the optical axis of the reconstructed image. Quality can be improved by recording two holographic images, obtained from different viewpoints simultaneously, and then combining holographic reconstruction with stereogrammatical viewing. Further improvements in image quality have been reported using phase conjugate playback, and compensation for aberration in the imaging system.

The off axis method uses separate optical paths for the object and reference beams and has the advantage of allowing reference and object beam intensity balancing to improve hologram quality. It has been shown that it is possible to collect the light scattered from the particles in two near-forward directions, allowing the recording of the holograms

at two time instants using two reference beams. Tracking the interrogation region through the reconstructed image produces a three-dimensional autocorrelation function.

### 1.5.3 Other PIV methods

By using parallel light sheets of different colors the cross sheet motion can be obtained from the color of the images [24,25]. The intensity distribution across a laser sheet may be used as a means of determining position by relating the image brightness to position [26]. The brightness dependence on other factors, such as particle size, means that technique using this approach need careful interpretation. The out-of-focus image size may be used as a depth indicator [27] as can the size and shape on the point-spread function from coded apertures [28]. High-speed movie recording of PIV scenes has enabled the estimation of the out-of-plane components by arguments of continuity [29].

Another development in this area is Forward Scattering PIV, a microscopic technique, that uses high-magnification forward-scattering information to yield 3D particle position information, though only within the instrument itself [30].

An Anglo-Mexican collaboration project recently invented a velocimetry method, which offers the potential for making simultaneous, global, multi-component velocity measurements and surface heat transfer/pressure meausurements. The method, called Tunnelling Velocimetry (TV), is currently undergoing advanced development and evaluation at the Centro de Investigaciones en Optica (CIO), Instituto Nacional de Astrofísica, Optica y Eléctronica (INAOE), and Photon Imaging (PI). TV is particularly attractive for application in both wind tunnel and flight testing environments due to its potential simplicity and global simultaneous measurement capabilities. The technique brings together much of the recent knowledge gained in optical metrology, diffraction

theory, luminescence barometry, thin films, and data analysis. A single instrument has been developed, capable of making real-time 3D fluid velocity and near-surface temperature/pressure optical measurements non-intrusively, simultaneously and instantaneously, using a single optical access point. Moreover, the method can potentially be extended to make fluid temperature, density and pressure measurements.

### 1.6 Concluding remarks

We have seen that PIV is a whole-field method for measuring fluid velocity, almost instantaneously. This approach combines the accuracy of single point methods with the multipoint nature of flow visualisation techniques.

We have also seen that PIV suffers from several major disadvantages. These include, among others, that the technique of dual-point optical access need, for orthogonal viewing, a thin light sheet that is intrinsically 2D. Alternative techniques for PIV three-dimensional investigation of fluid flows have been proposed, at the cost of increased complexity and optical access, and in some cases giving up a real-time measurement capability.

In an attempt to solve some of the above cited problems this thesis present the use of the GLMT and Fresnel approximation to the Huygens-Fresnel propagation theory for particle image calculation it is a novel contribution to three dimensional velocity measurements in these fields. Intensity and spatial information of a particle image diffraction pattern is used to calculate its three-dimensional position, and hence velocity information using real-time CCD cameras.

## References

1. R. J. Adrian, “Particle imaging techniques for experimental fluid mechanics”, Annual Review of Fluid Mechanics, **23**, pp. 261-304, (1991).

2. R. Meynart, “Equal velocity fringes in a Rayleigh-Bénard flow by speckle method”, Applied Optics, **19,** pp. 1385-1386, (1980).

3. R. J. Adrian, “ Scattering particle characteristics and their effect on pulsed laser measurements of fluid flow: speckle velocimetry vs particle image velocimetry, Applied Optics, **23,** pp. 1690-1691 (1984).

4. C. J. D. Pickering and N. A. Halliwell, “Laser speckle photography and particle image velocimetry: photographic film noise”, Applied Optics, **23,** pp. 2961-2969 (1984).

5. C. J. D. Pickering and N. A. Halliwell, “Speckle photography in fluid flows: signal recovery with two step proccesing”, Applied Optics, **23,** pp. 1128-1129 (1984).

6. R. Meynart, “Instantaneous velocity field measurements in unsteady gas flow by speckle velocimetry”, Applied optics, **22**, pp. 535-540 (1983).

7. R. J. Adrian and C. S. Yao, “Pulsed laser technique application to liquid and gaseous flows and the scattering power seed materials”, Applied Optics, **24**, pp. 44-52 (1985).

8. A. A. Adamczyk L. Rimai, "2-Dimensional particle tracking velocimetry (PTV): Technique and image processing algorithms", Experiments Fluids, **6**, pp. 373-380 (1988).

9. J. C. Agui and J. Jimenez, "On performance of particle tracking", Journal of Fluid Mechanics, **185**, pp. 447-468 (1987).

10. I. Grant and A. Liu, " Method for the efficiency incoherent analysis of particle image velocimetry images", Applied Optics, **28**, pp. 1745-1748 (1989).

11. M. F. Gallanzi, "High Accuracy Measurement of Unsteady flows using digital PIV", Optics and Laser Technology, **30**, pp. 349-359 (1998).

12. J. W. Goodman. Introduction to Fourier Optics. New York: McGraw Hill. 1968.G

13. R. J. Adrian, "Statistical properties of Particle Image Velocimetry measurements in Turbulent flow", Laser Anemometry in Fluids Mechanics-III (R. J. Adrian et al. Eds.), Lisbon: Technico Institute, pp. 115-129 (1988).

14. Y. C. Chao, "Digital image velocimetry", Applied Optics, **28**, pp. 740-748 (1989).

15. J. Soria, "An investigation of the near wake of a circular cylinder using a video-based digital cross-correlation Particle Image Velocimetry technique", Experiminetal Thermal Fluids Scientific, **12**, pp. 221-233 (1996).

16. T. Utami and T. Ueno, "Visualization and picture processing of turbulent flow", Experiments in Fluids, **2**, pp. 25-32 (1984).

17. B. J. Thompson, "Holographic methods for particle size and velocity measurement-recent advances", Holographic Optics II: Principle and Applications. Proccedings SPIE, **1136,** pp. 308-326 (1989).

18. T. P. Chang, N. Wilcox and G. B. Tatterson, "Application of image processing to the analysis of three-dimensional flow fields", Optical Engineering, **23,** pp. 283-287 (1984).

19. I. Grant and Y. Zhao, Y. Tan and J. N. Stewart, "Three component flow mapping: experiences in stereoscopic PIV and Holographic Velocimetry", Proceedings 4th International Conference in Laser Anemometry, Advances and Applications, ASME, pp. 365-371 (1991).

20. J. F. Delgado and M. L. Riethmuller, "Laser Speckle Velocimetry Three Dimensional Measurements", Project Report 1986-13 Von Karmen Institute for Fluid Dynamics, Rhode Saint Genèse, Belgium (1986).

21. P. Bryanston-Cross, "Whole Field Instantaneous 3-D PIV Measurements in Air" (1997 - SPIE's international symposium on optical Science Engineering, and Instrumentation, San Diego (USA) 27 July - 1 August 1997)

22. S. Ushijihama and T. Nobukazu, "Three Dimensional Particle Tracking with Laser-Light Sheet Scanning", Central Research Institute of Electric Power Industry (CRIEPI), Japan (1996).

23. B. Skarman, J. Becker and K. Wozniak, "Simultaneous 3D-PIV and temperature measurements using a new CCD based holographic interferometer", Flow Measurement and instrumentation, **7** (1), pp. 1-6 (1996).

24. T. Karurandani, M. Funakoshi and M. Oikawa, "Breakdown and Rearrangement of vortex streets in a far wake", Journal Physical Society of Japan, **58**(5), pp. 1597 (1989).

25. A. Cenedense and A. Paglialunga, "New technique for the determination of the third velocity component with PIV", Experiments in Fluids, **8,** pp. 228-230 (1988).

26. F. Dinkelacker, M. Schafer, W. Ketterle and J. Wolfrum, "Determination of third velocity components with PTA using an intensity graded light sheet", Experiments in Fluids, **13**, pp. 357-359 (1992).

27. W. Stolz and J. Kholer, “In plane determination of 3D-Velocity vectors using Particle Tracking Anemometry (PTA)”, Experiments in Fluids, **17**, pp. 105-109 (1994).

28. C. E. Willert and M. Gharib, “Three dimensional particle image with a single camera”, Experiments in Fluids, **12**, pp. 353-358 (1992).

29. O. Robinson and D. Rockwell, “Constructive of three-dimensional images of flow structure via Particle Tracking Techniques”, Experiments in Fluids, **14**, pp. 257-270 (1993).

30. M. F. Gallanzi, “Tunneling Velocimetry: consilience comes to the study of fluid dynamics”, Laser Anemometry in Fluids Mechanics-X (R. J. Adrian et al. Eds.), Lisbon: Technico Institute, (2000).

# Chapter 2

# Optimum velocimetry data display method to PIV

## 2.1 Introduction

The accuracy and detail demanded from PIV in the field of aerodynamics has been a major barrier to its practical application in the past. The approach of using the Gaussian profile for the particle images [1] to yield sub-pixel accurate position estimates has resulted in robust measurements being taken to an accuracy of 0.5% for the in-plane velocity in hostile industrial environments [2]. A further barrier to the practical use of PIV, is to convert its data into a format that is easy to use by a designer or researcher. With the raw data being randomly arranged, it has been difficult to display the data on a regular grid such that it may be compared with CFD (Computer Fluid Dynamics) or other measured data. The fundamental problem is that there is not an optimum algorithm for interpolating randomly sampled data.

Comprehensive work has been done to investigate the optimisation of PIV systems [3-12]. This meant studying a wide range of experimental and analysis methods. Due to the complex relationships implicated, the majority of previous work has involved computer simulation using *a priori* knowledge of at least some aspects of the velocity field under investigation. For instance, strictly speaking, optimum seeding density depends on pulse separation, number of pulses used, and analysis method. All have a number of user-defined parameters, velocity gradients, magnification, recording medium, signal-to noise ratio, etc.

Therefore, simplifying assumptions are taken to make the problem tractable. Results from these studies have produced a limited set of look-up criteria corresponding to a limited number of flow cases and data processing methods. A number of workers have addressed the issue of *a posteriori* optimisation of velocimetry data [viz. 13] but always from a particular data processing point of view, such as the application of bootstrapping and the modified weighted convolution method of interpolation. Since a large amount of data is typically obtained when carrying out practical velocimetry experiments, *a posteriori* optimisation is often required. In turbomachinery experiments for instance, the high cost of these facilities means that a large amount of data must be gathered in the shortest possible time, and analysed over perhaps many months to extract as much information as possible. Moreover, an optimum velocimetry data display method is required in applications involving Three-State Anemometry[14], which uses a combination of three monodisperse sizes of seeding to yield velocity, viscosity, and density by the differential paths of each seeding population. Temperature can be derived from the viscosity information, and by using the perfect-gas law, thermodynamic pressure can be inferred as well. This is a technique which aims to perform whole field, non-intrusive, instantaneous and simultaneous measurement of all four variables in fluid flow.

When analysing experimental data, one problem which needs to be addressed is: given a set of measurements, what is the finest grid, and therefore smallest detail, which can be reliably represented? Following Benzecri's second principle of data analysis: "The model must fit the data, not *viceversa"* [15], the only object form which a grid size estimate can be found is the data field itself.

In data fields with high velocity gradients, neither the correlation nor the particle tracking approach to velocimetry data processing are sufficient on their own. Therefore, combined correlation/tracking approaches have been developed where the image is first analysed using a correlation approach, and the information is then conveyed to a particle-tracking algorithm [16-18]. This type of algorithm is able to cope with both large changes in seeding density and high-turning flows with good accuracy (a particular implementation to super-resolution has been described elsewhere [19]). The software, known as AIP (Analysis by Integrated Processing), achieves high-accuracy position estimates for particle-tracking based on the concept of "locales" and the work of Havelock [2,20]. It also provides a bound for the smallest attainable Root-Mean-Square (RMS) position estimator error.

Loss reduction in turbomachinery is a major area of research. In this respect, studies on the relationship between viscous forces and loss generation [21] show that the entropy creation rate is likely to be high in regions where high velocities coincide with high viscous forces. This combination leads to high velocity gradients which result in varying seeding density, with areas of low velocity having low particle density and therefore high measurement error. High and uniform seeding densities can be obtained at high speeds but only in regions of low velocity gradients, which are not of major interest. Therefore, achieving and optimum seeding density throughout a complex flow field is difficult. Hence the need for an analysis code such as AIP. Low speed flows in air or water, on the other hand, can be assumed to have uniform seeding densities.

This chapter describes a novel analytical method to determine optimum interpolation data grid size for PIV, without any a priori knowledge of the fluid velocity field, data

processing method, or velocimetry system parameters. The research work presented here optimises experimental parameters without any particular analysis method or a priori velocity field information. Knowledge of the Kolmogorov scale is required, which does no involve the velocity field. Variables implicated in this novel method are: system magnification, seeding density, and Reynolds number. All can be optimised for any PIV system.

### 2.2 PIV Data Display Theory.

If PIV data is to be compared to a direct numerical simulation or other experimental measurements, the data must be displayed in a reliable and consistent form, independent of, for instance, the data processing method or system parameters. PIV recording gives randomly-sampled point measurements of a continuos flow field. If a fine grid is required to capture small scale features, in general, this implies a seeding density to be determined. There are two general forms to characterise PIV experiments, namely by the imaging system used and by the flow field velocity, each yielding complementary information.

#### 2.2.1 Imaging System: Magnification & Sensor Size.

For any given PIV system there exists a minimum velocity resolution $R$, given by the particle position accuracy which is currently of the order of $R = 0.1$ of a pixel for methods involving digital sub-pixel accuracy [1]. The largest feature which the system can record may be characterised by the size of the sensor. For instance, if the sensor is a conventional CCD-PAL camera, the sensor size is 768x576 pixels with a square pixel size of approximately 10 μm. Hence the ratio of the maximum to the minimum velocity

component which this particular sensor can record is approximately 5760, assuming a minimum resolution of 0.1 of a pixel related to the shortest sensor axis, given in terms of the total number of pixels $N_P$ in a sensor.

From a fluids standpoint, the smallest usable scale is that given by the Kolmogorov length scale. This is the smallest velocity scale which is considered to have a coherent structure, and therefore is useful to understand the flow field under investigation. The largest scale is directly related to the characteristic length, which in the case of flow past a cylinder, is the cylinder diameter. Moreover, the flow Reynolds number (based on cylinder diameter) to the 3/4 power is representative of the ratio of the largest to the smallest vortex:

$$L_k \approx \left( \frac{\nu^3 L_c}{\nu_c^3} \right)^{3/4}, \quad \frac{L_c}{L_k} = \mathrm{Re}^{3/4} \tag{1a}$$

$$L_k = R * L_{\substack{pixel \\ size}} * M^{-1}, \quad L_c = N_p * L_{\substack{pixel \\ size}} * M^{-1} \tag{1b}$$

where $M$, $L_k$, $L_c$, $L_{pixel\ size}$, $\nu$, $\nu_c$ are known as, the magnification, Kolmogorov scale, characteristic length, characteristic pixel size, viscosity, and characteristic velocity respectively. From the previous relations the Reynolds number can be related to the velocity resolution and total sensor pixel number,

$$\mathrm{Re} = \left[ \frac{N_p}{R} \right]^{4/3} \tag{2}$$

Thus, once a velocimetry system's velocity resolution is defined and the number of pixels available is known, the maximum flow Reynolds number attainable may also be determined. For a conventional CCD-PAL camera, the flow Reynolds number which can be measured in all its scales is at most 100,000. By considering the Kolmogorov scale, the optimum magnification of the system can also be derived, without any detailed knowledge of the fluid velocity field. The magnification must be such that velocity resolution matches the Kolmogorov length-scale. If the magnification is higher, the system will resolve random fluctuations which are of no interest for the reconstruction of the coherent velocity field. If magnification is too low, the system cannot resolve small scale velocity features. Conversely, knowing the flow Reynolds number the size of the sensor required can be found.

Since the magnification is given by matching the velocity resolution to the Kolmogorov length-scale, the sensor size is given by the imaging system and the experimental conditions such as viscosity/density/characteristic length are fixed, it follows that only the flow Reynolds number can be manipulated to bring the flow under study within the system's measurement capability.

### 2.2.2 Flow field velocity: grid size & seeding rate.

If an interpolated velocity field is analysed using a singular value decomposition then the first eigenvalue found for interpolated velocity field will correspond to the largest velocity vector, continuing until the smallest eigenvalue is reached corresponding to the smallest Kolmogorov scale. Further, some random eigenvalues will be found with scales lower than the Kolmogorov scale, but they can be considered negligible, because they do not contribute to velocity field information. Consider the ratio of the largest to the smallest

eigenvalues, this ratio is defined as the condition number of a matrix in 2-norm, which is defined as the largest eigenvalue. The concept of condition number can be used to define the minimum grid size on the basis of the experimental data.

The condition number also measures the stability of a data matrix and attempts to measure the worst possible effect caused when the velocity field is perturbed slightly. Thus, instability leads to large values of the condition number and *vice versa*. Turbulence, experimental errors, and numerical interpolation errors can be considered as a perturbing error function limiting the resolution of the measured velocimetry data field.

Velocity fields are in general continuos functions sampled at randomly distributed discrete points, subject to the resolution limitation previously described. An approximating PIV matrix can be constructed, for example, by an interpolation using the value or gradient of the value in any dimension [22]. The condition number of the approximating PIV data matrix depends on the number, distribution and accuracy of measurement points as well as on the flow field velocity gradient.

When interpolating, it is proposed that the approximating matrix condition number should be no larger than twice that of the original flow field matrix, to become a reliable and stable representation [23] of the original continuos field. Such a condition number, known as the condition limit, is equal to twice the ratio of the largest to smallest velocity scales, and it defines the minimum experimental grid size. If a grid size is selected too detailed for the experimental data obtained, then the condition number will rise above the condition limit. Thus, by applying the condition limit criteria data obtained from experiments carried out under different conditions can be compared directly.

Since the condition number of the approximating PIV data matrix is also influenced by seeding density, any variation of seeding through the flow field influences the grid size the data can be interpolated too. For instance, in a wake where there are high velocity gradients, the seeding rate might be orders of magnitude lower than those measured in free stream. As a first order approximation, seeding density can be considered to be directly proportional to speed. The latter leads to another problem in high velocity gradient fields: areas of high velocity have high measurement rates, while areas of low velocity, which are low accuracy areas, have low measurements rates. Therefore, given a PIV measurement, grid size can only be inferred from the data itself. Although this technique cannot predict the correct seeding rate to be used in an experiment, it can tell the user if the seeding rate employed was adequate or whether it needs to be increased to satisfy a given grid size requirement.

Figure 2.1 shows the algorithm used in obtaining the optimum grid for velocimetry interpolated data. PIV data is interpolated on an initial user-defined grid. Singular value decomposition (SVD) is applied to each interpolation matrix iteratively and smaller random singular values are filtered out using truncated singular value decomposition (TSVD) [24]. If the ratio between the largest singular value and the smallest valid one, which is the condition number in 2-norm, is close to twice the condition number of the fluid flow as given in equation 2, then this value is the

optimum grid. The iteration process stops when the grid is optimum.

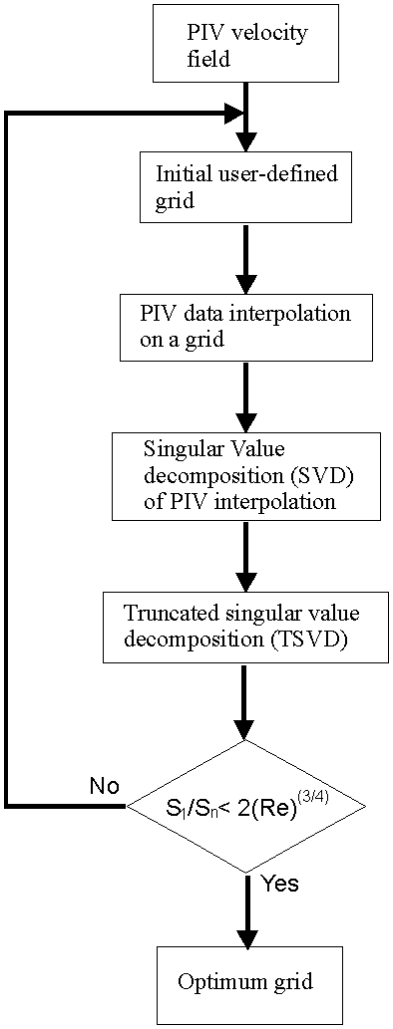


Figure 2.1. Optimum grid Algorithm

## 2.3 Modelled Flow and Discussion.

A CFD calculation of flow past the near wake of a cylinder at a Reynolds number of 140,000 is being used as test flow because experimental aerodynamic data is available for validation purposes [25]. Thus, the prediction produced as the primary velocity field for the research presented in this thesis, work was validated against it and found to be in good agreement, although it is only accurate to 0.01 of the variance. It should be pointed out

here that the lowest corresponding eigenvalues were ignored as these are basically random components of the velocity field. The CFD calculation used a Navier-Stokes second order scheme, Roe solver and the isothermal wall model. The turbulence model used was a k-e model, with wall laws. The CFD data was combined with a particle imaging representation based on the description in [26], and the image was then analysed. The experimental parameters considered were a cylinder of diameter 30mm with a mean flow velocity of 70 m/s. Figure 2.2 shows a plot of the flow being investigated. Once the velocity field is calculated, the question of the particle size to be employed as seeding remains unanswered. Based on previous work [27-29], it is known that the determining factor for accurate flow-following is the Stokes number:

$$St = \frac{\rho_p \quad \nu_c \quad d_p^2}{18\,\nu\,L_c} \tag{3}$$

where $\rho_p$ and $d_p$ represent particle density and particle diameter respectively the rest of the variable. For the particle to follow a flow accurately (to the order of 1% error) the Stokes number needs to be between 0.01 and 0.1. Thus, for this application, the particle diameter required is of the order of 2 μm. The particle size can then be inserted into a particle motion equation [30] to yield the particle velocity field.

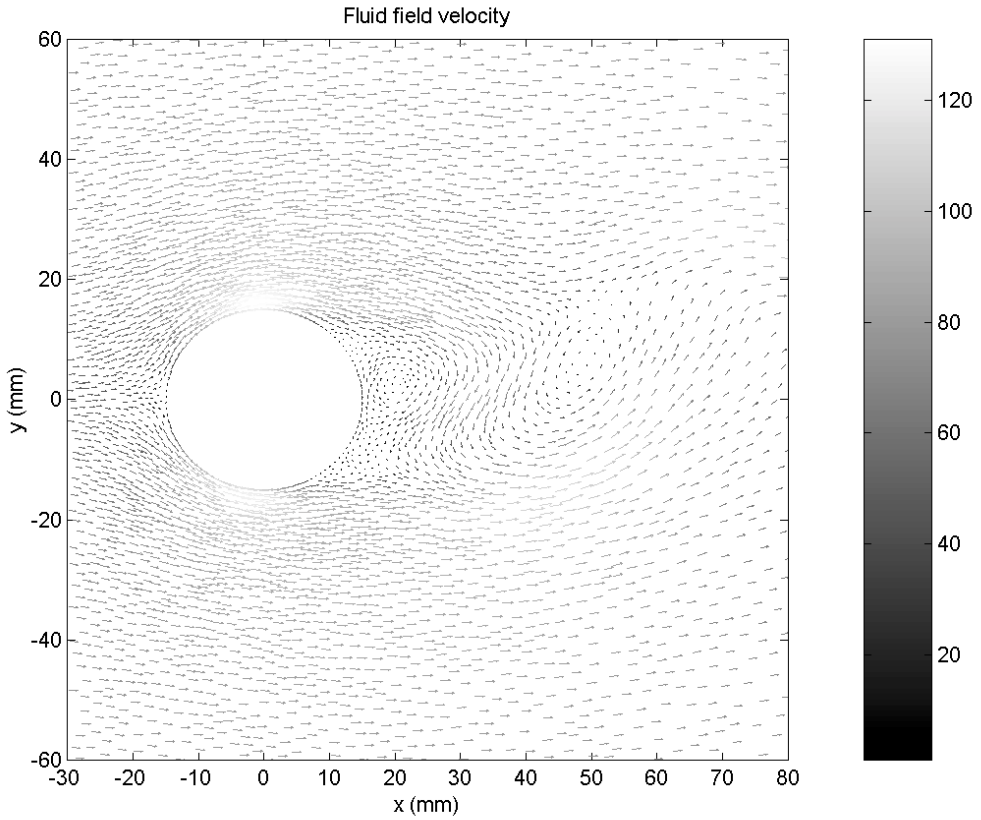


Figure 2.2. DNS of flow past a cylinder at Re = 140000

A 1024x1024, 8-bit digital CCD image with a pixel size of 10μm was simulated. The image contained 3,000 measurement points. This is the result of a seeding rate of 10 particles/mm$^3$ upstream. As a first order approximation, the local seeding density was set proportional to the flow velocity. The particle image included CCD noise. The CCD noise came from a real image at the conditions set in a Ludwieg tube. The particle imaging assumed a light-sheet thickness of 1mm. The simulation model assumed a frequency Nd:YAG laser with a wavelength of 532nm. The model also considered relative CCD camera (Pulnix TM-765) sensitivity at 532nm (80% of the peak) as opposed to peak sensitivity given at 600nm.

The region of interest, at a magnification of 0.25, was set to 40mm x 40mm at a distance of 600 mm, i.e., 1 mm behind the cylinder to provide a clearance in order to ensure that there would be no glare from laser light hitting the cylinder surface. A zoomed-in region of the image near the wake containing 100 measurements points is shown in figure 2.3.

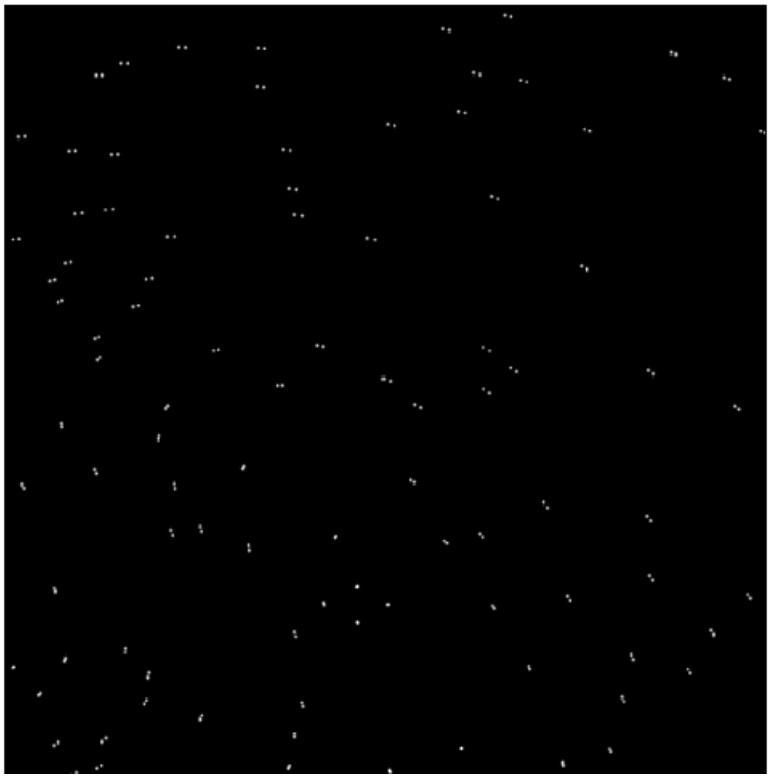

Figure 2.3 Zoomed-in PIV particle field

The simulated particle field was analysed using the AIP-PIV analysis package. In order to illustrate the effects of varying grid sizes on the error, Figure 2.4 shows grid size vs. normalised error, for the image shown in Figure 2.3. The grid size for which the error is a minimum corresponds to twice the condition number of the flow as shown by the theory

with a grid separation of 0.3 mm. This is explained by the fact that for a grid smaller than this amount, not all information is being displayed, while at grid sizes

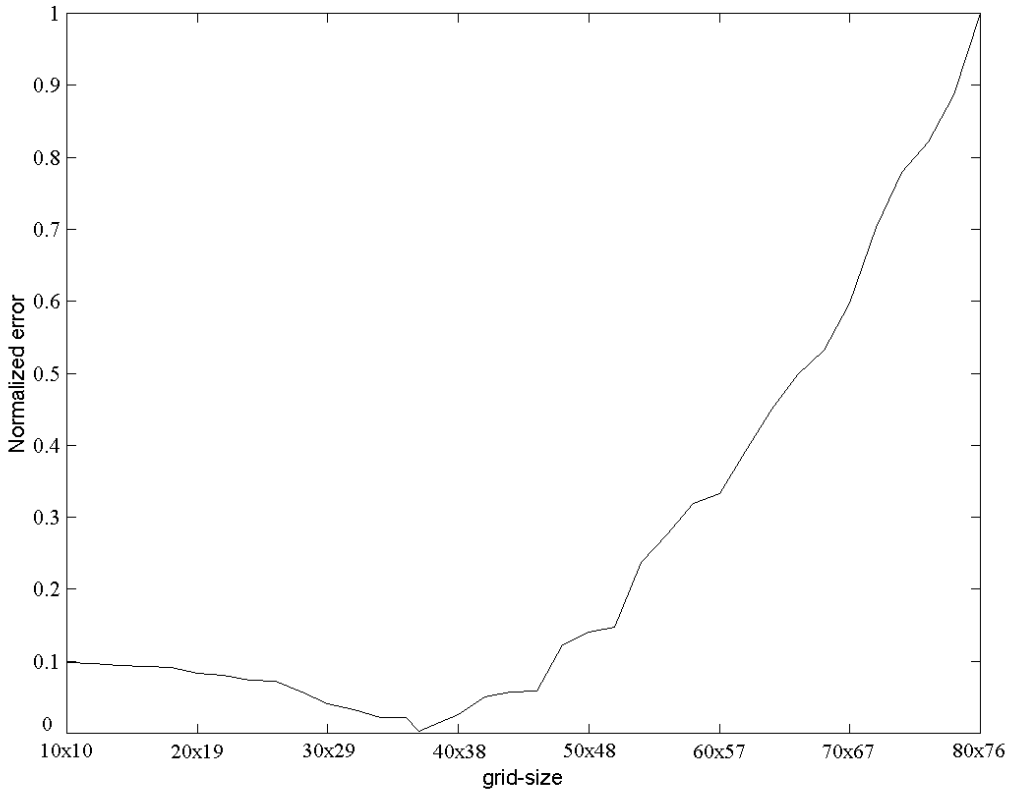


Figure 2.4 Grid separation vs. Normalised error

larger than this the condition limit is exceeded. Figure 2.5 shows the interpolated velocity field plotted using the optimum grid size, together with the PIV velocity measurements used to generate it. This figure illustrates the advantage of using PIV for unsteady flow research, i.e., using a comparatively small number of measurement points a detailed mesh of the underlying flow field can be derived. Thus, although PIV delivers a limited number of measurement points compared to Doppler Global Velocimetry, for instance, which

essentially yields a measurement per pixel, in general a high measurement data rate is not required to adequately reconstruct a flow field.

Conceptually the grid separation determined by the method presented here, can be considered to yield an estimate of the number of mesh points required to compute an equivalent field. Thus, for a resulting grid of 0.3 mm it is equivalent to having calculated a 40 mm field with 16,000 mesh points. Therefore, if PIV experimental data is to be compared to CFD data, the computation should be evaluated with this number of mesh points, which is much larger than the number of PIV measurement points.

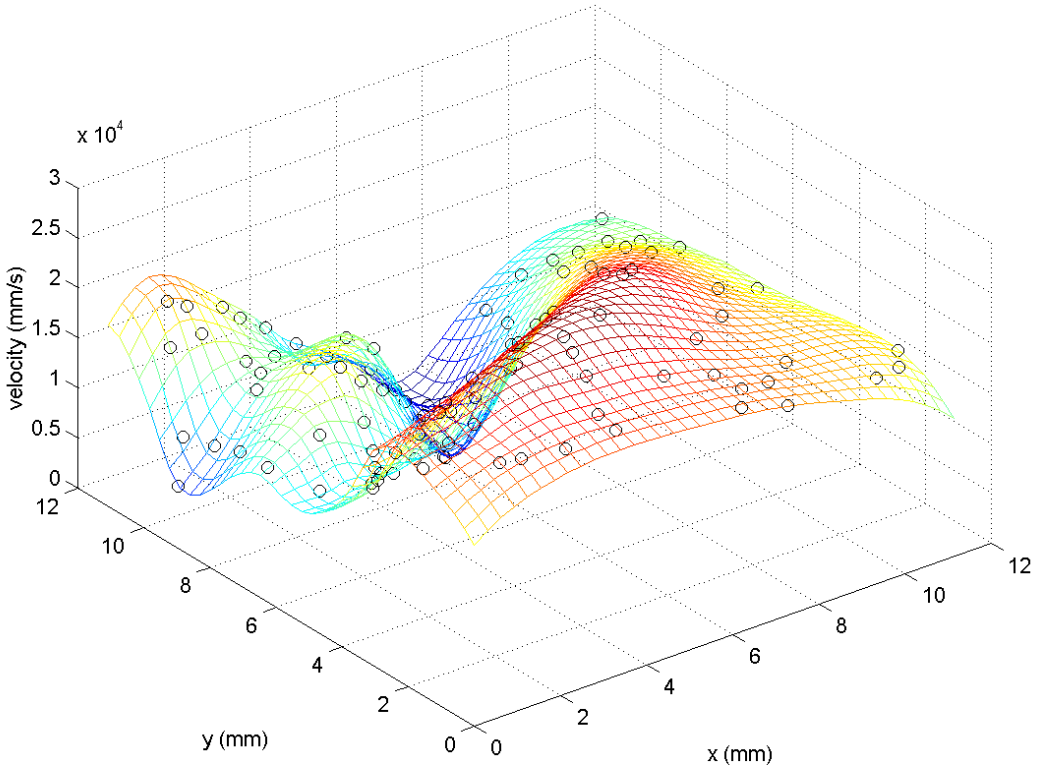


Figure 2.5 Interpolated velocity field mesh plot

## 2.4 An Experimental Example

The example was taken from a study of real-time measurements of velocity fluctuations in periodic and chaotic flows using Laser Doppler Velocimetry (LDV) and PIV [31] at a Reynolds number of 500, where LDV is also applicable. Velocity fluctuations were measured using a Laser Doppler Velocimeter, and amplitude measurements were taken in both smooth and baffled columns (internal diameter of 23 mm) in an oscillatory flow. The LDV results were supplemented with data from Particle Image Velocimetry. This information was used to illustrate oscillatory flow mechanisms in baffled tubes. Oscillatory flow has been used for many years in the field of chemical engineering. Chantry et al. [32] showed that pulsation improved mass transfer rates in packed and sieve-plate columns. Much of the early work quoted in a review paper by Baird [33] shows that the use of vibrations and pulsation are centred around separation processes (e.g. mineral/coal washing), liquid-liquid extraction, chemical reaction and fluidisation. Later, oscillatory flow found new uses in many areas. There are two parameters that are used to characterise an oscillatory flow namely, the Oscillatory Reynolds Number, $Re_o$, and the Strouhal Number, $St_o$, defined below:

$$\mathrm{Re}_o = \frac{\rho\, 2\pi\, f\, x\, d}{\mu} \tag{4}$$

$$St_o = \frac{d}{4\pi\, x} \tag{5}$$

where ρ is the fluid density, f is the frequency of oscillation, x is the center-to-peak amplitude of oscillation, $\mu$ is the absolute viscosity and d is the tube diameter.

The double-pulse digital PIV technique used in this study employed a pulsed frequency doubled Nd:YAG laser at a wavelength of 532 nm, with an energy of 150 mJ/pulse. The flow was seeded with the same particles as those used for the LDV experiments at a seeding density of approximately $7.5x10^5$ particles per ml. The baffles were made of Perspex to avoid reflections from the laser, which would interfere with the imaging optics. The K2 INFINITY diffraction limited optics was used for imaging, with a magnification factor of approximately 2 and a F/# Number of 22. The CCD cameras used were specially adjusted for laser operation. They were standard 768x576 CCD cameras with microlenses. The PIV investigation was limited to a study of a 60 wt. % aqueous solution of glycerol ($\mu$ = 0.0096 Pa. s, from measurements made on an RDS II rheometer using a 50 mm diameter parallel plate geometry at a gap of 0.25 mm). The specific gravity of the mixture was interpolated from Glycerol Viscosity Tables [34]. The oscillatory condition tested was for a frequency of 5 Hz and a centre to peak amplitude of oscillation of 5 mm.

The PIV system was housed inside a ventilated anechoic chamber. The oscillatory flow rig was set up inside the chamber and the tests were performed, the result shown in figure 2.6. This image shows the PIV optimum grid size normalised, and the interpolated data superimposed on the original image. The optimum grid size was found to be 45x33, with a condition number of 1000 just below twice the experimental Reynolds number at a magnification of 1.6x. The column is surrounded by a square Perspex box filled with deionised water, which helps to eliminate optical distortion. The oscillator is mounted on a 3D translation stage, and amplitude measurements can be made simultaneously with

velocity measurements by means of a purpose-built triggering device. The baffles used have one orifice, a constriction ratio of 50% and are space 3 tube radii (23 mm i.d.) apart.

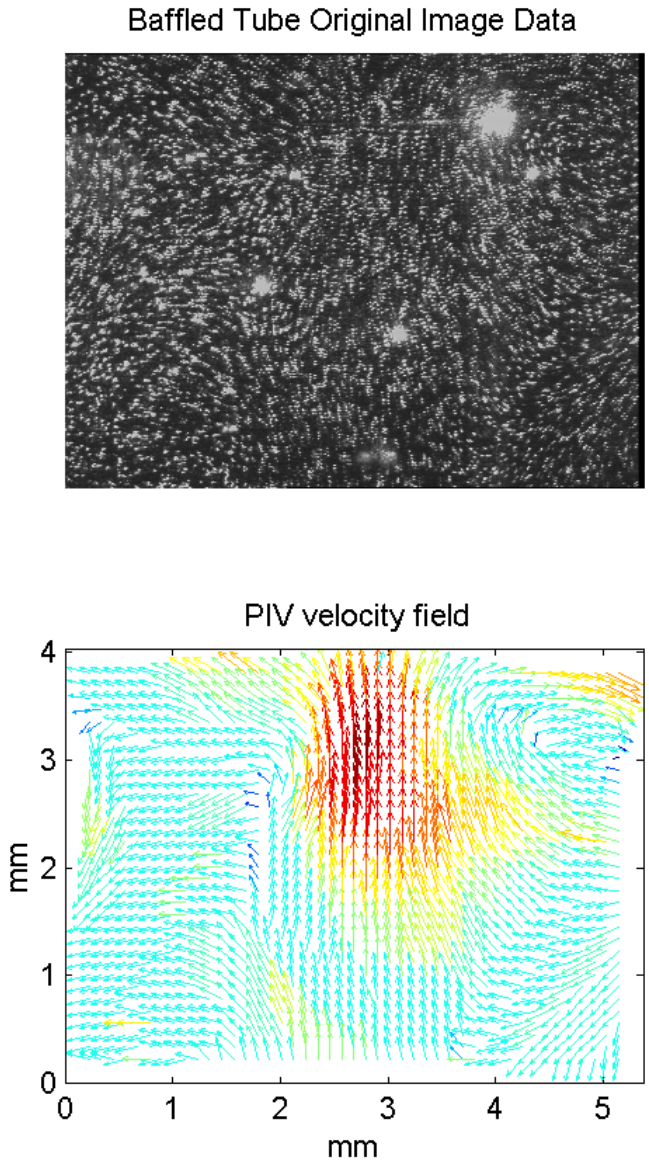


Figure 2.6 Baffled tube image and velocity field

## 2.5 Concluding remarks

There are three sets of independent constraints in PIV measurements which must be related. Firstly, the physical characteristics of the sensor with which the PIV image is to be recorded. Secondly, the range of scales in the velocity field under investigation (ranging from those of the same order as the characteristic length down to the Kolmogorov scale). Thirdly, once the data has been analysed and the velocity vectors calculated, the grid separation for an interpolated representation of the continuos field must be defined. The unifying concept for these three constraints is the condition number. The latter can be regarded as the ratio of the resolution to the largest sensor axis in the first case, the ratio of the characteristic length to the Kolmogorov scale in the second, and the sensitivity of the approximating matrix to perturbations in the third.

By setting the resolution to be equal to the Kolmogorov scale, the required sensor size and magnification are fixed and the first and second constraints are made consistent. The third constraint requires the determination of a grid separation which exhibits minimum error without detailed knowledge of the velocity field under investigation. This is achieved by setting the condition number of the interpolation to twice the condition number of the flow field. Finally, the calculated grid size requires the number of mesh points, which needs to be used to compare numerical calculations to experimental data.

## References

1. Funes-Gallanzi, M., Bryanston-Cross, P. J., & Udrea, D. D., "High accuracy Techniques Applied to the Extraction of Absolute Position Estimates in a 3DPIV System", VIIth Symposium on applications of Laser Techniques to Fluid Mech., Lisbon, (1994).

2. Funes-Gallanzi, M., "High Accuracy Measurement of Unsteady flows using digital PIV", Optics and Laser Technology, **30**, pp. 349-359, (1999).

3. Hinsch, K., Arnold, W., Platen, W., "Turbulence measurements by particle image velocimetry", L. I. A. 60 ICALEO, pp. 127-134, (1987).

4. Adrian, R. J., "Double exposure, multiple-field particle image velocimetry for turbulent probability density", Optics and Lasers in Engineering, **9**, pp. 211-228, (1988).

5. Coupland, J. M., Pickering, C. J. D., "Particle Image Velocimetry: estimation of measurement confidence at low seeding densities", Optics and Lasers in Engineering, **9**, pp. 201-210, (1988).

6. Keane, R. D., Adrian, R. J., "Optimisation of particle image velocimetry. Part I: doubled pulse systems", Measurement Science and Technology, **1**, pp. 1400-1402, (1990).

7. Grant, I. & Owens, E. H., "Confidence interval estimates in PIV measurements of turbulent flows", Applied Optics, **29**, pp. 1400-1402, (1990).

8. Prasad, A. K., Adrian, R. J., Landreth, C. C., Offutt, P. W., "Effect of resolution on the speed and accuracy of particle image velocimetry interrogation", Experiments in Fluids, **13**, pp. 105-116, (1992).

9. Boillot, Prasad, A. K., " Optimization procedure for pulse separation in cross-correlations PIV", Experiments In Fluids, **21**, pp. 87-93, (1996).

10. Lawson, N. J., Halliwell , N. A., Coupland, J. M., "Generalised Optimisation Method for Double Pulse particle image velocimetry", Optics and Lasers in Engineering, **27**, pp. 637-656, (1997).

11. Westerweel, J., " Fundamentals of Particle Image Velocimetry", Measurement Science and Technology, **8**, pp. 1379-1392, (1997).

12. Huang et al., "On errors of digital particle image velocimetry", Measurement Science and Technology, **8**, pp. 1427-1440, (1997).

13. Aguí, J. C., Jimenez, J., "On the performance of particle tracking", Journal of Fluid Mechanics, **185**, pp. 447-468, (1987).

14. Funes-Gallanzi, M., "A Numerical Investigation of Flow Past a Bluff Body Using Three-State Anemometry (3SA)", International Journal for Numerical Methods in Fluids, **26**, pp. 1023-1038, (1998).

15. Benzecri, J-P, et al, “L’Analyse des Donnees”, Tome 1: La Taxinomie, Tome 2: L’Analyse des Correspondances. Dunod, Paris, (1973).

16. Keane, R.D., Adrian, R.J., “Prospects for Super-Resolution with particle Image Velocimetry”, SPIE, **2005**, pp. 283-293, (1993).

17. Keane, R.D., Adrian, R.J., " for Super-Resolution particle Image Velocimetry”, Measurement Science and Technology, **6**, pp. 754-768, (1995).

18. E. A. Cowen and S. G. Monismith, "A hybrid digital particle tracking velocimetry technique", experiments in Fluids, **22**, pp. 199-211, (1997).

19. Funes-Gallanzi, M. and Mendoza Santoyo, F., “Analysis by Integrated Processing of Unsteady Flow PIV Data”, 1997 European Forum, The Royal Aeronautical Society, Wind Tunnels and Wind Tunnel Test Techniques, Cambridge, United Kingdom, April 14-16, 1997.

20. Havelock, D.I., “High precision position estimation in digital image metrology”, Ph.D. Thesis, Carleton University, Dept. Syst. Eng. Comput. Sci., Ottawa, Canada, July 1989.

21. Denton, J.D., “Loss Mechanisms in Turbomachines”, ASME 93-GT-435, (1993).

22. Sandwell, D.T., “Biharmonic spline interpolation of GEOS-3 and SEASAT altimeter data”, Geophysical Research Letters, **2**, pp. 139-142, (1987).

23. Atkinson, K.E., “An Introduction to Numerical Analysis”, Wiley, (1988).

24. Bertero, M. and Boccacci, P., "Introduction to inverse problems in imaging", Institute of Physics Publising Bristol and Philadelphia, pp. 220-263, (1998).

25. Cantwell, B., Coles, D., “An experimental study of entrainment and transport in the turbulent near wake of a circular cylinder”, Journal of Fluid Mechanics, **136**, pp. 321-374, (1983)

26. Adrian, R.J., “Particle-Imaging Techniques for Experimental Fluid Mechanics”, Annual Review of Fluid Mechanics, **23**, pp. 261-304, (1991).

27. Dring, R.P. & Suo, M., “Particle Trajectories in Swirling Flows”, AIAA Journal of Energy, **2**, No. 4, pp. 232-237, (1978).

28. Dring, R.P., "Sizing Criteria for Laser Anemometry Particles", Journal of Fluids Engineering, **104**, pp. 15-17, (1982).

29. Melling, A., “ Seeding gas flows for laser anemometry”, AGARD, CP-395, (1986).

30. Hinze, J.O., "Turbulence: An Introduction to its Mechanics and Theory", New York, McGraw Hill, pp. 352, (1959).

31. Hayden, E.S.S., Mackley, M.R., Neves-Saraiva, R.M.C. & Funes-Gallanzi, M., "Real-Time Measurements of Velocity Fluctuations in Periodic and Chaotic Flows using Laser Doppler Velocimeter and Particle Image Velocimetry", 5th World Congress of Chemical Engineering, AIChemE, IChemE and the European Federation of Chemical Engineering, San Diego, July, 1996.

32. Chantry, W.A., Berg, R.L. von and Weigandt, H.F., Ind. Eng. Chem., **47**, 1153 (1955).

33. Baird, M.H. I., Brit. Chem. Eng., **11**, 1, 20 (1966).

34. Sheely, M.L., Ind. Eng. Chem., **24**, 9,1060 (1932).

# Chapter 3

# Scattering theory of small spherical particle

## 3.1 Introduction

One of the most important elements in PIV is the small particle embedded in the flow field that scatters the light necessary to make velocity measurements. Particles are selected on the basis of their optical properties. They must scatter enough light to correctly expose the photographic material. Light scattering depends on particle shape and size, the refractive index of particles and fluid, and the polarization and wavelength $\lambda$ of the radiation.

Light interacts with matter by either elastic or inelastic scattering. Inelastic light scattering is known as Raman and fluorescent scattering. Inelastic light scattering is used as technique for identifying and determining the concentration of specific molecules. Inelastic scattering by molecules is considered as a collection of induced oscillating dipoles. The molecules are excited by the absorption of photons at the incident frequency. The electromagnetic fields inside the particle consist of a transmitted field at the incident frequency and secondary fields at other frequencies due to emissions by active molecules. Elastic scattering occurs when there is no exchange of energy between the incident light and the internal energy levels in the atoms. Elastic interactions are further subdivided into Raleigh and Mie

scattering, according to the size of the particles in relation to the illumination wavelength λ. The categories are defined as follow:

Rayleigh scattering $a << \lambda$

Mie scattering $a > \lambda$

Where $a$ is the particle diameter (particle assumed spherical).

Light scattering from spherical particles whose sizes are of the order of the wavelength has a exact solution from Maxwell's equations. The solutions of Maxwell's equations for a sphere in air was first given by Mie in 1908 [1] in an effort to understand the varied colors in absorption and scattering exhibited by small colloidal particles of gold suspended in water. About the same time Peter Debye [2] considered the problem of the radiation pressure exerted on small particles in space.

### 3.2 Classical Lorenz-Mie Theory (far-field case)

To study the scattering process theoretically, it is necessary to solve Maxwell's equations for the diffraction of a plane linearly polarized monochromatic wavefront, by a non-magnetic sphere embedded in a non-conducting homogeneous medium. The time independent Maxwell's equations for the electric and magnetic field are:

$$\nabla \times H = -ik\bar{n}^2 E \tag{3.1}$$

$$\nabla \times E = ikH \tag{3.2}$$

Where

$H$ magnetic field intensity

$E$ electric field intensity

$k$ wavenumber in vacuum

$\bar{n}$ complex refractive index

the Mie theory consists of finding the solution to Maxwell's equations, describing the field arising from a plane monochromatic wave incident upon a spherical surface, across which the properties of the medium change abruptly. An appropriate system of curvilinear coordinates is introduced and the field is represented as the sum of two subfields; one of the subfields is such that its electric vector has no radial component while the other has a magnetic vector with this property. In spherical polar coordinates Maxwell's equations together with the boundary conditions separate into a set of ordinary differential equations, which are then solved for the two subfields in the form of infinite series.

The Mie solution gives the field at any point inside and outside the particle. The resulting field components can be written in the form [3]:

$$E_\theta = -\frac{i}{k\tilde{r}} e^{-ik\tilde{r}+i\omega t} \cos\varphi S_2(\theta) \tag{3.3}$$

$$E_\varphi = \frac{i}{k\tilde{r}} e^{-ik\tilde{r}+i\omega t} \sin\varphi S_1(\theta) \tag{3.4}$$

where

$$S_1(\theta) = \sum_{n=1}^{\infty} \frac{2n+1}{n(n+1)} \{a_n \pi_n(\cos\theta) + b_n \tau_n(\cos\theta)\} \tag{3.5}$$

$$S_2(\theta) = \sum_{n=1}^{\infty} \frac{2n+1}{n(n+1)} \{b_n \pi_n(\cos\theta) + a_n \tau_n(\cos\theta)\} \tag{3.6}$$

$\pi$ and $\tau$ are the Legendre functions defined by

$$\pi_n(\cos\theta) = \frac{P_n^1(\cos\theta)}{sin\theta} \tag{3.7}$$

$$\tau_n(\cos\theta) = \frac{dP_n^1(\cos\theta)}{d\theta} \tag{3.8}$$

The scattering coefficients $a_n$ and $b_n$ are given by

$$a_n = \frac{\psi'_n(\bar{n}\alpha)\psi_n(\alpha) - \bar{n}\psi_n(\bar{n}\alpha)\psi'_n(\alpha)}{\psi'_n(\bar{n}\alpha)\xi_n(\alpha) - \bar{n}\psi_n(\bar{n}\alpha)\xi'_n(\alpha)} \tag{3.9}$$

$$b_n = \frac{\bar{n}\psi'_n(\bar{n}\alpha)\psi_n(\alpha) - \psi_n(\bar{n}\alpha)\psi'_n(\alpha)}{\bar{n}\psi'_n(\bar{n}\alpha)\xi_n(\alpha) - \psi_n(\bar{n}\alpha)\xi'_n(\alpha)} \tag{3.10}$$

where $\psi_n$, $\chi_n$, and $\xi_n = \psi_n - i\chi_n$ are the Riccati-Bessel functions, which are related to the Bessel functions of half-integer order; $P_n(\cos\theta)$ are the associated Legendre polynomials, depending uniquely on the observation direction. $\bar{n}$ is the complex refractive index of the sphere, and $\tilde{r} = r/a$ is the normalized distance from the particle to the scattered light observation point. All variables having the symbol ~ are normalized to the particle radius.

These fields, equations (3.3) and (3.4), represent an outgoing spherical wave with amplitude and state of polarization dependent in the direction of field traveling. The radial components $E_r$ and $H_r$ may also be derived from Mie's solution but tend to zero at higher powers of $1/r$.

Generally the computational problem involved in the Mie problem is to calculate the numbers:

$$i_1 = |S_1(\theta)|^2 \quad (3.11a)$$

and

$$i_2 = |S_2(\theta)|^2 \quad (3.11b)$$

where $i_1$ and $i_2$ represent the light intensity with its electric vector perpendicular and parallel to the plane through the direction of propagation of the incident light and to the scattering ligth viewpoint respectively.

Expressions 3.11a and 3.11b are employed to know the characteristics of Mie scattering. It can be illustrated by choosing a laser wavelength, e.g. 532 nm, and several particle sizes with a given index of refraction, e.g., 1.55 + 0j, corresponding to polystyrene particles. The particles scattering intensity is shown in Figure 3.1, for 0.2, 0.4, 1.0 and 4.0 μm diameter particle as a function of scattering particle. The complex nature and large dynamic range of the Lorenz-Mie scattering angle is easily seen. The general assumption that a larger particle will scatter more light greatly depends on the viewing angle.

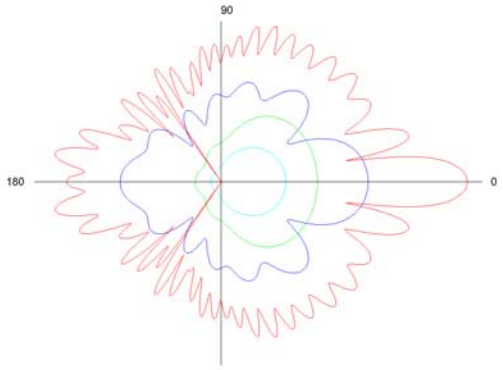


**Figure 3.1 Particle scattering intensity for 0.2, 0.4, 1.0 and 4.0 micron diameter particle as a function of scattering particle(cian-0.2, green-0.4, blue-1 and red-4).**

The intensity is in logarithmic scale and is plotted so that the intensity it is normalized to the maximum intensity of the largest particle. The Mie scattering can be characterized by the normalized diameter, $\alpha$, defined by:

$$\alpha = \frac{2\pi a_r}{\lambda}$$

If $\alpha$ is larger than unity, approximately $\alpha$ local maxima appear in the angular distribution over the range from 0º to 180º. For increasing $\alpha$ the ratio of forward to backward scatter intensity will increase rapidly. Hence, it would be advantageous to record in forward scatter, but, due to the limited depth of field, recording at 90º has often be used.

Mie theory, which assumes plane wave illumination, is unable to predict adequately the details of the far-field intensity of the scattered light. In response to this inadequacy of Mie theory, Gouesbet and his collaborators [4,5] devised a method to theoretically calculate the light scattered by a spherical particle that is illuminated by a polarized shaped beam. They found that the far-field intensity is determined by two sets of partial-wave amplitudes, the

usual plane wave Mie scattering amplitudes $a_n$ and $b_n$, and the partial-wave coefficients $g_{n,TM}$ and $g_{n,TE}$ of the incident field, as it will be seen in next section.

### 3.3 Generalized Lorenz-Mie theory

The Generalized Lorenz-Mie Theory (GLMT) gives the general expressions for electromagnetic scattering by spherical, homogeneous and isotropic scatters. In this section it is summarized, with the main results of the GLMT in their most general formulation given.

The problem under consideration is the scattering of a beam by a homogeneous and isotropic sphere. The scatterer is characterized by its diameter $a$ and its complex refractive index $\overline{n}$ with respect to a nonabsorbing surrounding medium. The wave is propagating along the z-axis, toward its positive direction. The location of the spherical particle relative to the incident field is arbitrary. A scattering theory for a spherical scatterer with arbitrary location in an arbitrary incident profile is given within the GLMT.

As a consequence of the spherical nature of the scatterer, the formulae of the GLMT will be given is spherical coordinates $(r,\theta,\varphi)$. The geometry used is defined in Figure 3.2. Consider two Cartesian co-ordinate systems ($O_g$uvw) and ($O_p$xyz) attached to the incident field and to the particle center, respectively. $O_g$u is parallel to $O_p$x and $O_g$v is parallel to $O_p$y. $O_g$ and $O_p$ is the beam waist centre and the particle centre, respectively. The incident field is linearly polarised, propagating toward the positive w axis with the electric field **E** parallel to the u axis. The scattered light is observed at point M'$(r,\theta,\varphi)$, where $r$, $\theta$, $\varphi$ are spherical co-ordinates attached to the particle system ($O_p$xyz).

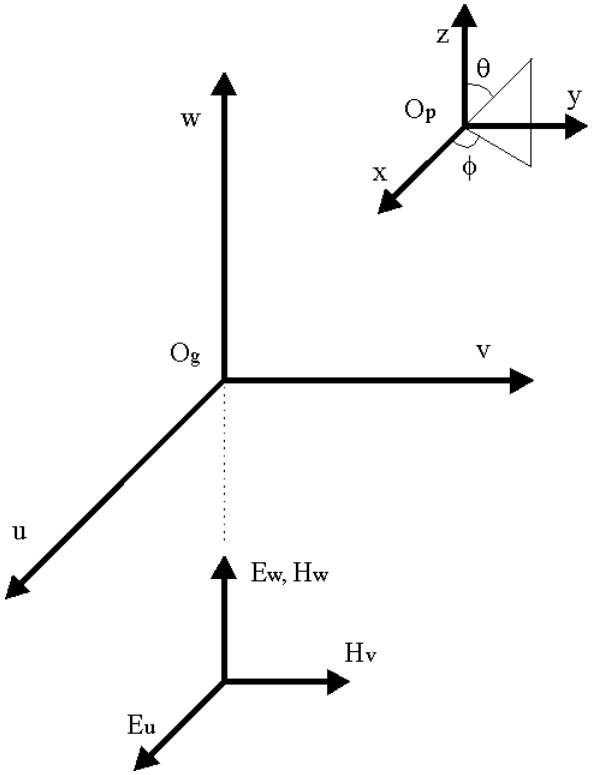


**Figure 3.2 System Geometry for GLMT calculations.**

### 3.3.1 Bromwich description of the incident shaped beam

Starting from Maxwell's equations, the general electromagnetic field can be expressed as the combination of two special, linearly independent solutions: the Transverse Magnetic (TM) and the Transverse Electric (TE). In the Bromwich formulation [5-9 ], the six field components of each special solution are expressed from two Bromwich Scalar Potentials (BSP), $U_{TM}$ and $U_{TE}$, complying with the same second order partial derivative equations.

The Bromwich formulation is valid with the assumption that the coordinate system $(x_1,x_2,x_3)$ is an orthogonal curvilinear one whose basis $(e_1,e_2,e_3)$ complies with:

$$\frac{\partial e_1}{\partial x_2} = \frac{\partial e_1}{\partial x_3} = 0 \tag{3.12}$$

*and*

$$\frac{\partial\left(\frac{e_2}{e_3}\right)}{\partial x_1} = 0 \tag{3.13}$$

In the special case of time-harmonic waves and spherical coordinates, the differential equation for BSP's can be solved by variable separation, and the BSP's are found to be linear combinations of products of Ricatti-Bessel functions by spherical surface harmonics $Y_n^m(\vartheta,\varphi)$. We express these functions in terms of spherical Bessel functions $\Psi_n^j(kr)$ and associated Legendre polynomials $P_n^m(\cos\vartheta)$ (with the notation $P_n^0 = P_n$ for the basic Legendre polynomials). So the general expressions of the BSP's are the following [10]:

$$U_{TM} = E_0 \sum_{n=1}^{\infty} \sum_{m=-n}^{+n} \frac{1}{k} i^{n-1} (-1)^n \frac{2n+1}{2n(n+1)} g_{TM}(n,m,j) r \Psi_n^{(j)}(kr) P_n^{|m|}(\cos\theta) \exp(im\varphi) \tag{3.14}$$

$$U_{TE} = H_0 \sum_{n=1}^{\infty} \sum_{m=-n}^{+n} \frac{1}{k} i^{n-1} (-1)^n \frac{2n+1}{2n(n+1)} g_{TE}(n,m,j) r \Psi_n^{(j)}(kr) P_n^{|m|}(\cos\theta) \exp(im\varphi) \tag{3.15}$$

where $E_0$ and $H_0$ are the field amplitudes, $k$ is the wavenumber, while $g_{TM}$ and $g_{TE}$ are coefficients characterizing the incident field profile.

There are four spherical Bessel functions (j=1,2,3,4), but only $r\Psi_n^1(r)$ is defined at the coordinate center (i.e. $r$=0), and only $r\Psi_n^4(r)$ gives an outgoing spherical wave in the limit $r\rightarrow\infty$. According to physical considerations, one then chooses the best-suited function and obtains the expressions of the incident BSP's $U_{TM}^i$ and $U_{TE}^i$. Once the BSP's will be known, the TM and TE field components may be obtained. Thus, before obtaining the field components, the last step to get the BSP's of the incident wave is to compute the $g_{TM}$ and $g_{TE}$ coefficients. These coefficients can be obtained from the radial field components $E_r(r,\theta,\varphi)$ and $H_r(r,\theta,\varphi)$, by identifying of two independent expressions for these radial components. Firstly, from the TM and TE definitions we have $E_{r,TE}$=$H_{r,TM}$=0, giving

$$E_r(r,\theta,\varphi)= E_{r,TM} \tag{3.16}$$

$$H_r(r,\theta,\varphi)= H_{r,TE} \tag{3.17}$$

Secondly, from the BSP's definitions we also have two basic relations $E_{r,TM}(H_{r,TE})$ and $U_{TM}^j(U_{TE}^j)$. Hence assuming known expressions for $E_r(r,\theta,\varphi)$ and $H_r(r,\theta,\varphi)$ we can deduct $g_{TM}(n,m,j)$ and $g_{TE}(n,m,j)$. For instance, the electric radial component would read:

$$E_r(r,\theta,\varphi) = E_0\sum_{n=1}^{\infty}\sum_{m=-n}^{+n}\frac{1}{k}i^{n-1}(-1)^n\frac{2n+1}{2n(n+1)}g_{TM}(n,m,j)\frac{n(n+1)}{r}\Psi_n^{(j)}(kr)P_n^{|m|}(\cos\theta)\exp(im\varphi) \tag{3.18}$$

### 3.3.2 Expressions of the $g_{TM}$ and $g_{TE}$ coefficients for a given incident field profile

Assume $E_r(r,\theta,\varphi)$ and $H_r(r,\theta,\varphi)$ are known. They will be used to find the coefficients for $g_{TM}(n,m,j)$ and $g_{TE}(n,m,j)$. Assumed also that the incident wave is defined at, the scatter

center point (0,0,0). Thus we choose $\Psi_n^1$ in the BSP's expressions (3.14 -3.15), and the coefficients to calculate, for simplicity will now be written $g_{n,TM}^m$ and $g_{n,TE}^m$. The calculating of the above coefficients may be given by spherical harmonic expansions, results given as quadratures.

Whenever the *r*-variable can be separated from $\theta$ and $\varphi$ in the $E_r$ and $H_r$ expressions, it is possible to expand $E_r$ and $H_r$ in spherical harmonics of the first kind. The expansion theorem is valid for any $f(\theta,\varphi)$ function, provided that itself and its two first derivatives are continuos. We then obtain for the electric field:

$$E_r = E_0 \sum_{n=0}^{\infty} \sum_{m=-n}^{+n} C_{n,TM}^m P_n^{|m|}(\cos\theta) \exp(im\varphi) \tag{3.19}$$

with

$$C_{n,TM}^m(r) = \frac{(2n+1)}{4\pi} \frac{(n-|m|)!}{(n+|m|)!} \int_0^{2\pi} \int_0^{\pi} \frac{E_r(r,\theta,\varphi)}{E_0} P_n^{|m|}(\cos\theta) \exp(-im\varphi) sin\theta d\theta d\varphi \tag{3.20}$$

The spherical harmonics are a complete set of orthogonal functions, so we identify the coefficients in both expressions for $E_r$ (Eqs. 3.18 and 3.19) and obtain:

$$g_{n,TM}^m = C_{n,TM}^m(r) \frac{r}{\Psi_n^{(1)}(kr)} \frac{1}{n(n+1)C_n^{pw}} \tag{3.21}$$

Apparently from their definition, the coefficients $g_{n,TM}^m$ do not depend on *r*, however they do. Its *r*-dependence in (3.21) may be known by using the operator $\int_0^{\infty} r\Psi_n^{(1)}(kr)d(kr)$ and the orthogonality relations for spherical Bessel functions, leading to:

$$g_{n,TM}^{m}(r)=\frac{(2n+1)k}{i^{n-1}(-1)^{n}2\pi^{2}}\frac{(n-|m|)!}{(n+|m|)!}\int_{0}^{2\pi}\int_{0}^{\pi}\int_{0}^{\infty}\frac{E_r(r,\theta,\varphi)}{E_0}r\Psi_n^{(1)}P_n^{|m|}(\cos\theta)\exp(-im\varphi)sin\theta d\theta d\varphi \tag{3.22}$$

The case of the $g_{n,TE}^{m}$ coefficients is similar to the *TM* ones, employing *H* and *TE* instead of *E* and *TM*.

### 3.3.3 Scattering from a spherical scatterer

From the previous section, the Bromwich description of the incident wave is known. Let us now consider the scattering of this wave by a sphere with diameter *a* and complex refractive $\overline{n}$, centered on the coordinate system of Figure 3.2. The idea is to express the BSP's for the scattered and for the sphere waves. From BSP's, the external and sphere fields will then be derived and, finally all the scattered quantities characterizing the scattering process, similarly as for the classical Lorenz-Mie theory.

The external and sphere BSP's $U_{TM}^{e}$, $U_{TE}^{e}$, $U_{TM}^{sp}$ and $U_{TE}^{sp}$ have the general form of equations 3.14 and 3.15 with, j=4 and j=1 respectively, as explained early. The exact expressions for the coefficients are obtained from the tangential continuity of the electromagnetic field at the sphere surface ($a_r$=$a$/2 or $2\pi r/\lambda=\alpha$, size parameter). From here one calculates the six components of each wave and obtain the field everywhere inside and outside the scatterer.

The scattering field components in the near field are described [5] as:

$$\tilde{E}_r^{(s)} = -\sum_{n=1}^{\infty}\sum_{m=-n}^{+n} a_n g_{n,TM}^m \left(\xi_n(\alpha\tilde{r}) + \xi_n''(\alpha\tilde{r})\right) P_n^{|m|}(\cos\theta)\exp(im\varphi), \tag{3.23}$$

$$\tilde{E}_\theta^{(s)} = -\frac{1}{\alpha\tilde{r}}\sum_{n=1}^{\infty}\sum_{m=-n}^{+n} \left[a_n g_{n,TM}^m \xi_n'(\alpha\tilde{r})\tau_n^{|m|}(\cos\theta) + mb_n g_{n,TE}^m \xi_n(\alpha\tilde{r})\Pi_n^{|m|}(\cos\theta)\right]\exp(im\varphi), \tag{3.24}$$

$$\tilde{E}_\phi^{(s)} = -\frac{i}{\alpha\tilde{r}}\sum_{n=1}^{\infty}\sum_{m=-n}^{+n} \left[ma_n g_{n,TM}^m \xi_n(\alpha\tilde{r})\Pi_n^{|m|}(\cos\theta) + b_n g_{n,TE}^m \xi_n(\alpha\tilde{r})\tau_n^{|m|}(\cos\theta)\right]\exp(im\varphi). \tag{3.25}$$

where $a_n$ and $b_n$ are the usual scattering coefficients of the Lorenz-Mie theory give by equations 3.9 and 3.10, $\xi_n$ is a Ricatti-Bessel functions, $\xi_n'$ its derivative, $\tau_n^{|m|}$ and $\Pi_n^{|m|}$ are generalized functions defined by:

$$\tau_n^m(\cos\theta) = \frac{d}{d\theta}P_n^m(\cos\theta) \tag{3.26}$$

$$\Pi_n^m(\cos\theta) = \frac{P_n^m(\cos\theta)}{\sin\theta} \tag{3.27}$$

with the notation $\tau_n^1 = \tau_n$ and $\Pi_n^1 = \Pi_n = \pi_n$ corresponding to equations 3.7 nd 3.8.

There are applications where the interest is limited to the so called far field, defined by the inequality $r >> \lambda$. So, the functions $\xi_n(kr)$ are simply expressed as $\xi_n(kr)=i^{n+1}\exp(-ikr)$. Consequently, the scattered wave becomes transverse ($E_r=H_r=0$), with [5]:

$$\tilde{E}_\theta^{(s)} = -\frac{i}{\alpha\tilde{r}}\exp(-ikr)\sum_{n=1}^{\infty}\sum_{m=-n}^{+n}\frac{2n+1}{n(n+1)}\left[a_n g_{n,TM}^m \tau_n^{|m|}(\cos\theta) + imb_n g_{n,TE}^m \Pi_n^{|m|}(\cos\theta)\right]\exp(im\varphi), \tag{3.28}$$

$$\tilde{E}_\phi^{(s)} = -\frac{1}{\alpha\tilde{r}}\exp(-ikr)\sum_{n=1}^{\infty}\sum_{m=-n}^{+n}\frac{2n+1}{n(n+1)}\left[ma_n g_{n,TM}^m \Pi_n^{|m|}(\cos\theta) + ib_n g_{n,TE}^m \tau_n^{|m|}(\cos\theta)\right]\exp(im\varphi). \tag{3.29}$$

Now the $g_n^m$ coefficients are beam shape dependent and are specific to GLMT, characterising of the incident beam, i.e., beam dependent: beam waist diameter, wavelength and $O_g$-co-ordinate u, v, w. These beam coefficients can be numerically evaluated by using quadrature techniques [11], which are, however, time-consuming, preventing extensive applications. After significant work with the use of finite series [12], the best method has been found to arise from so-called localized approximation [13] for on-axis Gaussian beams, later successfully generalized to off-axis Gaussian beams [14] without any rigorous justification, which was eventually produced for both on-axis and off-axis beams [15,16]. The localized approximation allows to speed up the evaluation of beam shape coefficients by orders of magnitude, when compared with the earlier quadrature techniques.

Although a rigorous justification exists only for Gaussian beams, the localized approximation has been empirically found to be remarkably efficient for other kinds of beams, namely, laser sheets [17], top hat beams [18], and doughnut laser beams [19]. This leads to the conjecture that the localized approximation is actually valid for arbitrarily shaped beams [20]. Therefore, this method is used in this thesis by utilizing expressions found [17] previously.

The technique used to compute the Ricatti-Bessel functions and $a_n$, $b_n$ coefficients is described elsewhere [21]. Computation of the associated Legendre function is accomplished by using standard recursion formulas such as those presented by Abramowitz and Stegun [22]. All electric field quantities are normalized based on an assumed uniform incident electric field of unit amplitude.

### 3.4 Incident field

We are interested in calculating light scattering by spherical particles in forward, side and backward scatter directions. In the forward direction, the observed field is not only the scattered field but a total field obtained by adding up the incident field and the scattered field. Moreover, the radial electric field component of the incident field profile is needed to calculate the $g_n^m$ coefficients. Here, we will only give the incident field expression for a light sheet, and from light sheet expressions derive Gaussian and the planewave incident field.

The incident field for a light sheet is given by, viz. [23]:

$$\tilde{E}_r^{(i)} = \varphi_0^{sh}\left[(\cos\phi)\sin(\theta)\left(1-\frac{2Q_x}{\tilde{l}_x}\tilde{r}\cos\theta\right)+\frac{2Q_x}{\tilde{l}_x}\tilde{x}_0\cos\theta\right]\exp(K) \tag{3.30}$$

$$\tilde{E}_\theta^{(i)} = \varphi_0^{sh}\left[\cos\phi\left(\cos\theta+\frac{2Q_x}{\tilde{l}_x}\tilde{r}\sin^2\theta\right)-\frac{2Q_x}{\tilde{l}_x}\tilde{x}_0\sin\theta\right]\exp(K) \tag{3.31}$$

$$\tilde{E}_\varphi^{(i)} = -\varphi_0^{sh}\sin\varphi\exp(K) \tag{3.32}$$

where,

$$K = -i\alpha\left(\tilde{r}\cos\theta-\tilde{z}_0\right) \tag{3.33}$$

$$\varphi_0^{sh} = (-Q_xQ_y)^{1/2}\exp\left[-\frac{iQ_x}{\tilde{\omega}_{0x}^2}(\tilde{r}\cos\phi\sin\theta-\tilde{x}_0)^2-\frac{iQ_y}{\tilde{\omega}_{0y}^2}(\tilde{r}\sin\phi\sin\theta-\tilde{y}_0)^2\right], \tag{3.34}$$

$$Q_x = \frac{1}{i + (2/\tilde{l}_x)(\tilde{r}\cos\theta - \tilde{z}_0)} \tag{3.35}$$

$$Q_y = \frac{1}{i + (2/\tilde{l}_y)(\tilde{r}\cos\theta - \tilde{z}_0)}, \tag{3.36}$$

$$\begin{aligned} \tilde{l}_x &= \alpha\tilde{\omega}_{0x}^2 \\ \tilde{l}_y &= \alpha\tilde{\omega}_{0y}^2 \end{aligned} \tag{3.37}$$

$\tilde{\omega}_{ox}$ and $\tilde{\omega}_{oy}$ are the beam waist radii in the x and y directions, respectively. The incident field for a Gaussian beam may be recovered as a special case from a laser sheet when $\tilde{\omega}_{0x} = \tilde{\omega}_{0y}$, and for a wave plane by allowing $\tilde{\omega}_{0x}$ and $\tilde{\omega}_{0y}$ to become large.

Expresions 3.28 and 3.29 are useful to illustrate the differences among the three illumination shaped beams. Figure 3.3 shows the intensity distribution as a function of the viewing angle for a particle of diameter 4 μm, using the GLMT. According to figure 3.3, at 0º (forward scattering) and 180º (back scattering) the distribution is symmetrical for a given ratio in three co-ordinates, so the calculation for the particle diffraction pattern is easier to perform than it is at 90º or 270º (side scattering), The latter shape distribution of the diffraction pattern is not symmetrical and the calculation needs to be performed for each

point in the aperture and the radial symmetry simplification does not apply. Moreover, figure 3.3 shows the differences in intensity between viewing positions and illumination shaped beams.

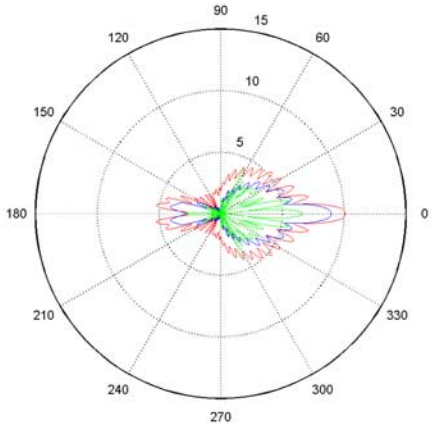


**Figure 3.3 The normalized scattering pattern for a glass particle 4μm in diameter suspended in air, obtained using plane wave (red), Gaussian (blue), and light sheet (green) shaped beams.**

### 3.5 Concluding remarks

We have given the classical Lorenz-Mie Theory (LMT) and the Generalized Lorenz-Mie Theory (GLMT). The LMT gives the general expressions for electromagnetic scattering by spherical, homogeneous and isotropic scatterers by using waveplane illumination. The GLMT deals with a scattering theory for a spherical scatterer with arbitrary location illuminated by an arbitrary incident beam profile, such as a laser beam or a ligth sheet. The electric field scattered by the spherical small particle is used to calculate the particle image.

### References

1. G. Mie., "Bietrage zur Optik trüber Medien, speziell kolloidaler Metallosungen", Annual Physics, 25, pp. 377-445, (1908).

2. P. Debye, "Der Lichtdruck auf Kugeln von beliebigem Material", Annual Physics, 30, pp. 57-136, (1909).

3. H. C. Van de Hulst, Light scattering by small particles, Wiley, New York (1957).

4. G. Gouesbet, G. Grehan and B. Maheu, “Scattering of a gaussian beam by a Mie scatter center using a Bromwich formulation”, Journal Optics, **16**(2), pp. 83-93 (1985).

5. Gousbet, G., Maheu, B., Gréhan, G., "Light Scattering from a sphere arbitrarily located ina Gaussian beam, using a Bromwich formulation", Journal Optical Society of America A, 5, pp. 165-176, (1994).

6. G. Gouesbet, G. Grehan and B. Maheu, “The order of approximation in a theory of the scattering of a gaussian beam by a Mie scatter center”, Journal Optics, **16**(5), pp. 239-247 (1985).

7. G. Grehan, “Theorie de Lorenz-Mie et applications a la granulometric optique (1985). These d’etat, 19 dec. 1985, Rouen, France.

8. G. Grehan, B. Maheu and G. Gouesbet, “Scattering of laser beams by Mie scatter centers: Numerical results using a Localized approximation”, Applied Optics, **25**(19), 3539-3548 (1986).

9. B. Maheu, G. Grehan and G. Gouesbet, “Generalized Lorenz Mie Theory: Firs exact values and comparisons with the localized approximation”, Applied Optics, **26**(1), 23-25 (1987).

10. T. J. Bromwich, “Electromagnetics waves”, Philos. Mag., **38**, pp. 143-164 (1919).

11. Gouesbet, C. Letellier, K. F. Ren, and G. Gréhan, "Discussion of two quadrature methods of evaluating beam shape coefficients in generalized Lorenz-Mie theory", Applied Optics, 35, pp. 1537-1542, (1996).

12. Gouesbet, G. Gréhan, and B. Maheu, "Expressions to compute the coefficients gnm in the generalized Lorenz-Mie theory, using finite series", Journal Optics (Paris), 19, pp.35-48 (1998).

13. G. Gréhan, B. Maheu, and G. Gouesbet, "Scattering of laser beams by Mie scatters centers: numerical results using a localized approximation", Applied Optics, 25, pp. 3539-3548, (1986).

14. G. Gouesbet, G. Gréhan, and B. Maheu, "A localized interpretation to compute all the the coefficients gnm in the generalized Lorenz-Mie theory ", Journal Optical Society of America A, 7, pp. 998-1007, (1990).

15. J. A. Lock and G. Gouesbet, "Rigorous justification of the localized approximation to the beam shape coefficients in generalized Lorenz-Mie theory. I. On-axis beam", Journal Optical Society of America A, 11, pp. 2503-2515, (1994).

16. G. Gouesbet and J. A. Lock, "Rigorous justification of the localized approximation to the beam shape coefficients in generalized Lorenz-Mie theory. II. Off-axis beam", Journal Optical Society of America A, 11, pp. 2516-2525, (1994).

17. K. F. Ren, G. Gréhan, and G. Gouesbet, "Evaluation of laser laser-sheet beam shape coefficents in generalized Lorez-Mie theory by use of a localized approximation", Journal Optical Society of America A, 11, pp. 2072-2079, (1994).

18. G. Gouesbet J. A. Lock, and G. Gréhan, "Partial wave representation of laser beams for use in light scattering calculation", Applied Optics, 34, pp. 2113-2143, (1995).

19. K. F. Ren, G. Gouesbet, and G. Gréhan, "The integral localized approximation in generalized Lorenz-Mie theory", Applied Optics, 37, pp. 4218-4225, (1998).

20. G. Gouesbet, "Validity of the localized approximation for arbitrary shaped beams in the generalized Lorenz-Mie theory for spheres", Journal Optical Society of America A, 7, pp. 1641-1650, (1999).

21. Dave, J.V., “Scattering of Electromagnetic radiation by a large, absorbing sphere”, IBM Journal of Research & Development, 13(3), pp. 302-313, (1969).

22. Abramowitz, M., Stegun, I.A., eds., "Handbook of Mathematical Functions", pp. 332-334, Dover, New York, (1972).

23. K. F. Ren, G. Gréhan and G. Gouesbet, "Electromagnetic field expression of a laser sheet and the order of approximation", Journal Optics (Paris), **25**(4), pp. 165-176, (1994).

# Chapter 4

# Image calculation of a small spherical particle

## 4.1 Introduction

In this chapter we will give the theory for the electric field propagation to the image plane. The electric field can be propagated to the image plane through the use of the Fresnel propagation equation. The derivation of the theoretical model relies on several assumptions that simplify the analytical approach. The model also includes Seidel aberrations of a typical lens used for velocimetry, such as a 90mm SIGMA Macro, such that the accuracy of the model is improved, and thereby increasing the accuracy of the particle positioning algorithm. It is the spherical and coma form of aberrations that play a major role, and therefore it was these the ones included in the model.

## 4.2 Approximated image calculation.

In general the particle image intensity is given by the square of the magnitude of the convolution resulting from camera lens system point response function and the geometric image of the particle. The contents of these functions determine the precise shape and diameter of the blurred image.

Adrian & Yao [1] first proposed using a quadrature to derive a nominal particle image diameter $d_e$ according to:

$$d_e = \sqrt{(M^2 d_p^2 + d_s^2)} \tag{4.1}$$

where

$$d_s = 2.44(M+1)\lambda f/\# \tag{4.2}$$

is the diameter of the point response function of a diffraction-limited lens measured at the first dark ring of the Airy disk intensity distribution (Fig. 1). The particle diameter is $d_p$, the wavelength is $\lambda$, the focal length of the lens divided by the aperture diameter is *f*/#, and *M* is the imaging system magnification. As defined here, $d_s$ is also equal to twice the mean diameter of a laser speckle. Equation (4.1) is an approximate quadrature representing the combined effects of magnification and image blurring in determining the final diameter of the image. If the point response function and the geometric paraxial image distribution were both Gaussian,

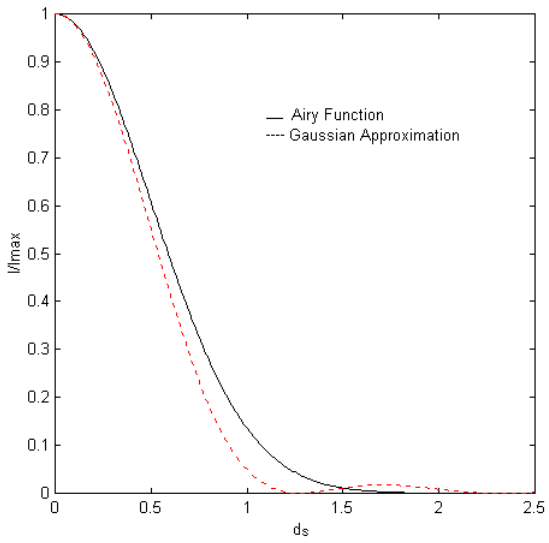


Figure 4.1 Image plane intensity distribution

this equation would be exact. In fact a Gaussian distribution has been used in the past as an adequate approximation to the Airy distribution, as shown in Fig. 1. Hence, equation (4.1) has been used as an approximation, assuming the paraxial image distribution is not too different from a Gaussian. This approach represents a compromise between paraxial optics and a simplified approximation to the Lorenz-Mie Theory. The former approach is only valid when the wavelength of the light used is much smaller than the scatterer size and for light beams close to the imaging system optical axis, while the latter is only valid when the particle is illuminated by a plane wave. The plane wave assumption holds when the size of the scatterer is small enough with respect to the characteristic dimensions of the incident beam, but in many cases this condition is not satisfied. Even if the plane wave assumption holds in a velocimetry set-up, the orientation of this wave-front relative to the viewing camera generally changes substantially across the field of view such that major corrections are required for each particle's scattering image. An accurate analysis of the field must rely on the Generalized Lorenz-Mie Theory (GLMT) for any position in the illuminated field.

Simplifications in formulating the physical problem to be solved were evaluated, such as considering a particle to be a point function. However, that treatment does not consider a particle's complex refractive index, representative laser power, or the different intensity distributions exhibited by particles that are an equal distance out of focus but on opposite sides of the focal plane. This last aspect being of crucial importance in making a modeling approach worthwhile, since if a particle position behind of and in front of the focal plane cannot be distinguished, such an approach would be severely deficient.

Therefore, a theoretical model was initially devised which allows calculation of the image produced by a spherical absorbing particle illuminated by monochromatic light,

including the amount of light energy falling onto the CCD sensor.

### 4.3 Exact Image Calculation

The specific imaging system under consideration has been described in detail in previous work done by other authors [2,3], and can be seen simplified in Figure 2. This system was used as a starting point in order to validate our software. In this system, an object located at plane $z_0$ is illuminated by a Nd:YAG or a He-Ne laser. The image is formed by passing the scattered light through a plano-convex lens (f=50 mm, D=25mm) onto a sensor (plane $z_3$), from where the image is sent to a frame grabber.

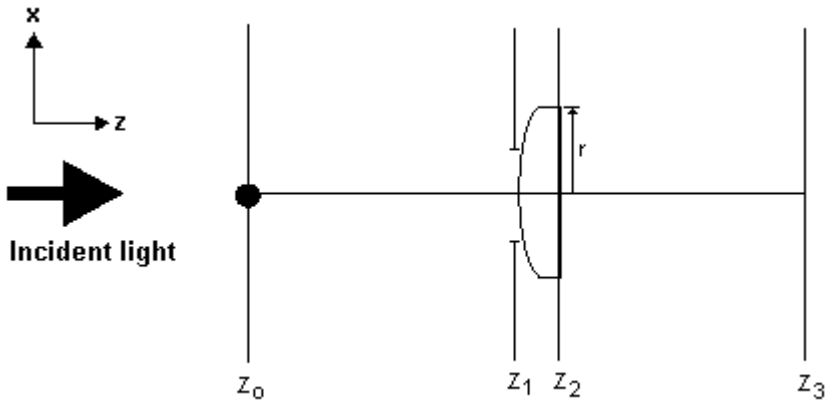


Figure 4.2 Initial layout.

The general approach to the theoretical model, which is outlined in this section, can be summarized in three steps. The first step is to calculate the x component of the external

electromagnetic field resulting from the interaction of the incident field with the particle using the exact series expressions presented in an earlier paper by Gouesbet et al. Appropriate phase shifts are then introduced, as a second step, to the portions of the external electric fields that are collected by the aperture and imaging lens. After passing through the imaging lens, third step, the electric field can then be propagated to the image plane through the use of the Fresnel propagation equation.

Assuming that the laser/droplet interaction can be modeled as a linearly polarized plane wave incident on a spherical absorbing particle, the electromagnetic field distribution can be obtained everywhere using classic Lorenz-Mie Theory [36,37]. Equations from this theory yield exact knowledge of the electromagnetic field at every point within the aperture located at plane $z_1$.

In addition, the actual physical problem depicted in Fig. 2 can be simplified based on several experimental observations. Diffraction effects due to the aperture may be neglected for the aperture size of 8mm used in the imaging system, so the aperture only serves to decrease the effective lens diameter and hence increase the f/#. As the aperture size becomes small, however, this assumption is no longer valid. The mathematical details incorporating the above discussion are presented below, with an extension to GLMT for velocimetry applications.

The propagation of the field from the imaging lens to the image plane is accomplished using scalar diffraction theory. For the particle case being considered, the x component of the external electric field is assumed to be the dominant field component transmitted through the imaging system. This assumption can be verified by direct computation of the external field components, and is physically reasonable since the incident field has dominant polarization in the x direction. A great deal of previous work

has examined the validity of using scalar theory in modeling the propagation of electromagnetic energy [4-8]. In particular, the use of the Fresnel approximation to the Huygnes-Frenel equations has received considerable attention because of the computational advantage it provides. The use of the Fresnel approximation, however, imposes certain restrictions over the range in which one can expect accurate results. In this work, the criterion of Goodman [9] has been used, which states that the Fresnel approximation may be used, provided the distance $z_{32}$ satisfies the relation:

$$z_{32}^3 = (z_3 - z_2)^3 >> \frac{\pi}{4\lambda}\left[(x_3 - x_2)^2 + (y_{3-} y_2)^2\right]_{max}^2 \tag{4.3}$$

Let the x-component of the external electric field be $E_m$, where the subscript refers to the field evaluated at plane $z_m$. As discussed in chapter 3, the electric field at plane $z_1$ is known exactly from Generalized Lorenz MieTheory. $E_2$ can be related to $E_1$ by assuming that the paraxial thin lens expression is valid,

$$E_2(x_2, y_2) = \exp(iknΔ_o)\exp\left[-\frac{ik}{2f}(x_1^2 + y_1^2)\right]E_1(x_1, y_1) \tag{4.4a}$$

where $f$ is the focal length of the lens, $\Delta_o$ is the thickness of the lens, $n$ is the lens refractive index, $k=2\pi/\lambda$ is the wave number, and $x_{1,2}$, $y_{1,2}$ are coordinates axes set on plane at $z_1$ and $z_{2,}$ respectively. By thin lens, we mean that the thickness of the lens is such that a light ray enters and leaves the lens at essentially the same $x$-$y$ co-ordinates, thus making $(x_1,y_1)$ and $(x_2,y_2)$ interchangeable, then

$$E_2(x_2,y_2)=\exp(ikn\Delta_o)\exp\left[-\frac{ik}{2f}(x_2^2+y_2^2)\right]E_1(x_2,y_2), \tag{4.4b}$$

Note that the lens in the imaging stem is assumed to be ideal and free from any aberrations. Using the Fresnel approximation in proceeding from plane $z_2$ to $z_3$,

$$E_3(x_3,y_3)=\frac{\exp[ik(z_3-z_2)]}{i\lambda(z_3-z_2)}\iint_A E_2(x_2,y_2) \times\exp\left\{\frac{ik}{2(z_3-z_2)}\left[(x_3-x_2)^2+(y_3-y_2)^2\right]\right\}dx_2dy_2. \tag{4.5}$$

Where $A$ is the integrating area at plane $x_1$, $y_1$. Substituting Eq. (4.4b) into Eq. (4.5),

$$E_3(x_3,y_3)=\frac{\exp[ik(z_3-z_2)]}{i\lambda(z_3-z_2)}\iint_A \exp(ikn\Delta_o)\exp\left[-\frac{ik}{2f}(x_2^2+y_2^2)\right]\times E_1(x_2,y_2) \times\exp\left\{\frac{ik}{2(z_3-z_2)}\left[(x_3-x_2)^2+(y_3-y_2)^2\right]\right\}dx_2dy_2. \tag{4.6}$$

For convenience, Eq. (4.6) can be written in spherical (r,ϕ) coordinates (i.e., $x_m = r_m\cos\phi_m$ and $y_m = r_m\sin\phi_m$, for plane $z_m$),

$$E_3(r_3,y_3)=\frac{\exp[ik(z_3-z_2)]}{i\lambda(z_3-z_2)}\int_0^{2\pi}\int_0^{ra}\exp(ikn\Delta_o) \times\exp\left\{-\frac{ik}{2f}\left[(r_2\cos\phi_2)^2+(r_2 sin\phi_2)^2\right]\right\}E_1(r_2,\phi_2) \times\exp\left\{\frac{ik}{2(z_3-z_2)}\left[(r_3\cos\phi_3-r_2\cos\phi_2)^2+(r_3 sin\phi_3-r_2 sin\phi_3)^2\right]\right\}r_2dr_2d\phi_2 \tag{4.7}$$

.

Based on experimental observations discussed earlier, the assumption for a field symmetry about the $z$ axis is used, i.e., $E_1(r_2,\phi_2)=E_1(r_2)$. Also, since only the intensity will be considered at plane $z_3$, constant phase factors can be omitted giving,

$$E_3(r_3,\phi_3)=\frac{1}{i\lambda(z_3-z_2)}\int_0^{r_a}E_1(r_2)r_2\exp(-\frac{ik}{2f}r_2^2)$$
$$\times\int_0^{2\pi}\exp\left\{\frac{ik}{2(z_3-z_2)}\left[r_3^2+r_2^2-2r_2\cos(\phi_2-\phi_3)\right]\right\}d\phi_2 dr \tag{4.8}$$

In addition to simplifying the electric field description, the $z$ symmetry axis assumption also allows exact evaluation of the angular integral in Eq. (4.8). Utilizing orthogonality along with the identity

$$\exp(iasinx)=\sum_{k=-\infty}^{\infty}J_k(a)\exp(ikx) \tag{4.9}$$

equation (8) can be simplified, giving

$$E(r_3)=\frac{2\pi}{i\lambda(z_3-z_2)}\exp\left[\frac{ikr_3^2}{2(z_3-z_2)}\right]\int_0^{r_a}E_1(r_2)J_0(\beta) \tag{4.10}$$
$$\times\exp\left\{-\frac{ikr_2^2}{2}\left[\frac{1}{f}-\frac{1}{(z_3-z_2)}\right]\right\}r_2 dr_2,$$

where $J_o$ is zero order Bessel function of the first kind, and

$$\beta=\frac{kr_2r_3}{(z_3-z_2)}. \tag{4.11}$$

The intensity at the image plane can be written from eq. (4.10),

$$I_3(r_3) = E_3(r_3)E_3^*(r_3)$$
$$= \left[\frac{2\pi}{\lambda(z_3 - z_2)}\right]^2 \left| \int_0^{r_a} E_1(r_2) J_o(\beta) \exp\left\{ -\frac{ikr_2^2}{2}\left[\frac{1}{f} - \frac{1}{(z_3 - z_2)}\right]\right\} r_2 dr_2 \right|^2 \tag{4.12}$$

where the asterisk denotes the complex conjugate. To remain consistent with the Lorenz-Mie Theory development, Eq (4.12) is written in terms of dimensionless variables,

$$\tilde{I}_3(\tilde{r}_3) = \left[\frac{\alpha}{(\tilde{z}_3 - \tilde{z}_2)}\right]^2 \left| \int_0^{r_a} \tilde{E}_1(\tilde{r}_2) J_o(\tilde{\beta}) \exp\left\{ -\frac{i\alpha\tilde{r}_2^2}{2}\left[\frac{1}{f} - \frac{1}{(\tilde{z}_3 - \tilde{z}_2)}\right]\right\} \tilde{r}_2 d\tilde{r}_2 \right|^2 \tag{4.13}$$

where

$$\tilde{\beta} = \frac{\tilde{r}_2 \tilde{r}_3 \alpha}{(\tilde{z}_3 - \tilde{z}_2)},$$
$$\tilde{r} = \frac{r}{a}, \quad \tilde{z} = \frac{z}{a}, \quad \tilde{f} = \frac{f}{a}. \tag{4.14}$$

### 4.4 Particle image diffraction with aberrations

In the presence of aberrations the image of a particle is distorted. In this case the image may be found by including a phase term in equation 4.4b. The amplitude $E_2(x_2,y_2)$ including the phase distribution, may be expressed as

$$E_2(x_2,y_2)=\exp(ikn\Delta_o)\exp\left[-\frac{ik}{2f}(x_2^2+y_2^2)\right]E_1(x_2,y_2)\exp(ikW(x_2,y_2)), \tag{4.15}$$

For this case, $W(x_2,y_2)$ is the wavefront shape in the presence of the optical system aberrations. Here for completeness, it is shown the five forms of aberrations through the following equation in cartesian coordinates:

$$W(x_2,y_2)=F+Ey_2+D(x_2^2+y_2^2)+C(x_2^2+3y_2^2)+By(x_2^2+y_2^2)+A(x_2^2+y_2^2)^2 \tag{4.16}$$

In polar coordinates we may write this polynomia as

$$W(r_2,\phi_2)=F+E\tilde{r}_2\cos\phi+D\tilde{r}_2^2+C\tilde{r}_2^2(1+\cos^2\phi)+B\tilde{r}_2^3\cos\phi+A\tilde{r}_2^4 \tag{4.17}$$

where the coefficients given indicate aberrations for:

$A$ = Sphericity.

$B$ = Coma.

$C$ = Astigmatism.

$D$ = Defocusing.

$E$ = Tilt about the $x$ axis.

$F$ = Constant or piston term.

### 4.5 Concluding remarks

Propagation of the electric field through the imaging system components is developed from a scalar viewpoint using the thin-lens transformation and the Fresnel approximation to the

Huygens-Fresnel propagation equation. The model also includes Seidel aberrations of the optical system used, such that accuracy of the model is improved, and thereby increasing the accuracy of the particle positioning algorithm. Although the theoretical model presented has been simplified extensively over the actual physical problem, the results agree qualitatively with experimental observations.

**References**

1. Adrian, R.J., Yao, C.S., “Development of Pulsed laser velocimetry for measurement of fluid flow”, in Proceedings, Eighth biennial Symposium on Turbulence, G. Patterson & J.L. Zakin, eds., University of Missouri, Rolla, (1983).

2. Wiles, K.J., "Development of a system for secondary liquid injection into a Mach 2 supersonic flow to study drop size and distribution by video imaging techniques", Master's thesis, University of Nebraska, Lincoln, (1985).

3. Schaub, S.A., Alexander,D.R., Barton, J.P., "Theoretical model for the image formed by a spherical particle in a coherent imaging system: comparison to experiment", Optical Engineering, 23(5), pp. 565-571, (1989).

4. W. Goodman, "Introduction to Fourier Optics", McGraw-Hill, New York, (1968).

5. J. E. Harvey, “Fourier treatment of near-field scalar diffraction theory”, American Journal Physics, **47**, pp. 974-980 (1979).

6. F. D. Feoick, “Wave propagation in optical system with large apertures”, Journal Optical Society of America, **68**, pp. 485-489 (1978).

7. J. C. Heurtley, “Scalar Rayleigh-Sommerfeld and Kirchhoff diffraction integrals: A comparison of exact evaluation for axial point”, Journal Optical Society of America, **63**, pp. 1003-1008 (1978).

8. H. G. Kraus, “Huygens-Fresenel-Kirchhoff wave-front diffraction formulation: spherical waves”, Journal Optical Society of America, A **6**, pp. 1196-1205 (1989).

# Chapter 5
# Results and discussions

## 5.1 Introduction

The results obtained when using the theory given in chapters 3 and 4 are presented and discussed in this chapter. The image particle is obtained when using both the Generalized Lorenz-Mie Theory to calculate the scattered field from the spherical particle (equations 3.23-3.25), and the Huygens-Fresnel theory to propagate the electric field to the image plane (equation 4.13). As shown in section 4.4 the theoretical model may include the aberrations of the optical imaging system (the spherical aberration has a clearer effect in image calculation).

The whole purposes is to get high exactitude for the two dimensional particle position, and exploit spatial and intensity particle image information to extract depth particle position. Then, three dimensional velocity measurements can be obtained in PIV.

As seen this thesis throughout, a specific analysis is carried out in order to get accuracy model of particle images to agree with their corresponding experimental conditions, as well as to show that the analytical model is correct. The application of this model to measure a velocity flow field is described by Guerrero et al [1].

## 5.2 Comparison between GLMT and Gaussian approximation

In general it can be said that the light scattered by a small particle is a function of the ratio of the refractive index of the particle to that of the surrounding medium, and the particle size, their shape and orientation. These properties are ignored by PIV in the particle image calculation. A Gaussian particle image approximation has been done now, causing

obviously particle image centre position errors. Figure 5.1 shows a low magnification (2x) particle image

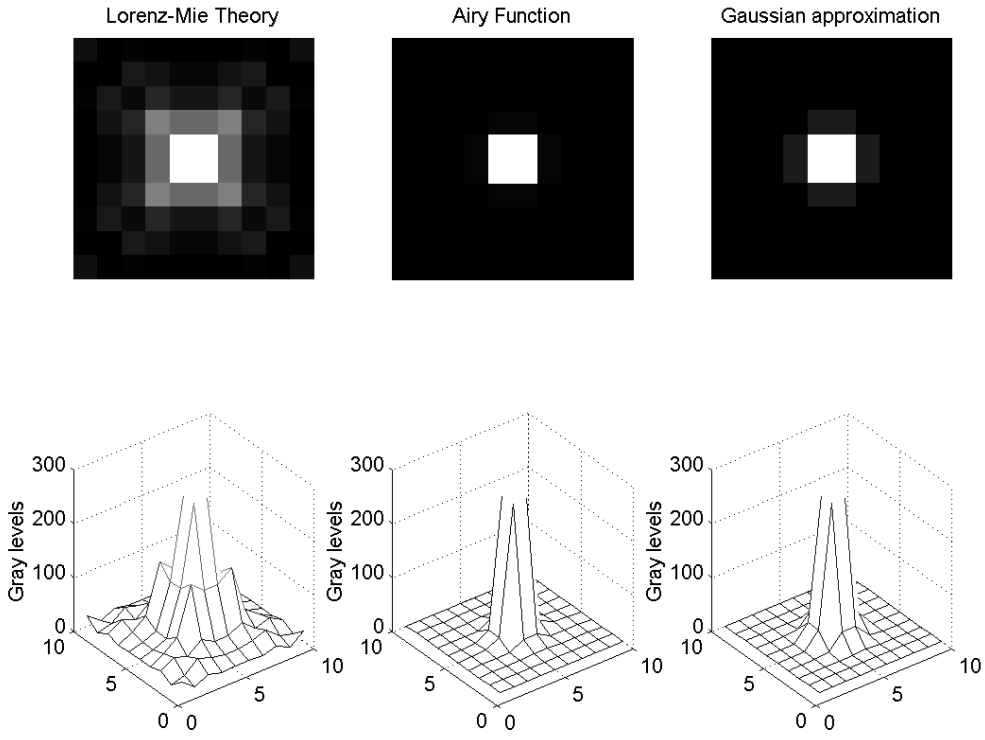


Figure 5.1 Three different modelled calculations of a particle image, at low magnification (2x)

simulation of an 18 μm diameter glass particle, with He-Ne laser illumination, and using three different models for particle imaging. Indeed, it is clear the difference in the gray level intensity; this information can be used to improve particle centre estimation and to increase particle position accuracy.

The spatial information can be seen in the three-dimensional plot from the Lorenz-Mie Theory, figure 5.2. In the 2D image the spatial information is lost due to the difference between high and low pixel intensity. With a CCD (charged coupled device) it is possible to cut the maximum pixel intensity in the image particle by adjusting its gain setting.

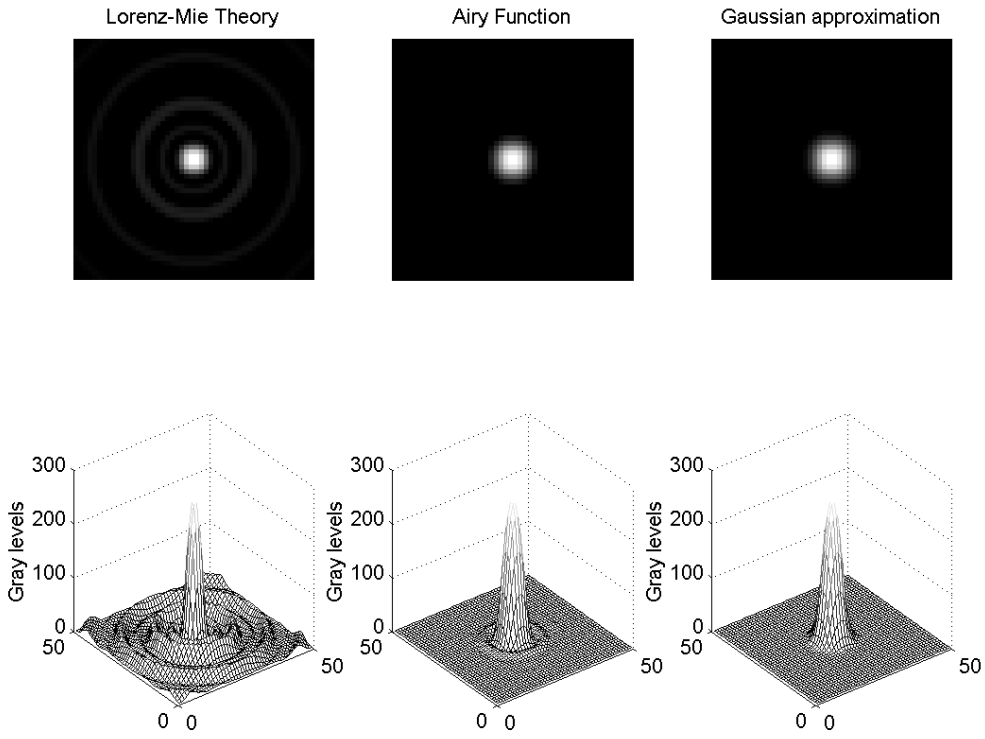


**Figure 5.2 Three different modelled calculations of a particle image, at 7.85x magnification**

Figure 5.3 shows a particle image adjusted to 5 percent of its maximum intensity. The difference in spatial information is clear between the three models. This spatial information can be used to estimate the depth position of the particle.

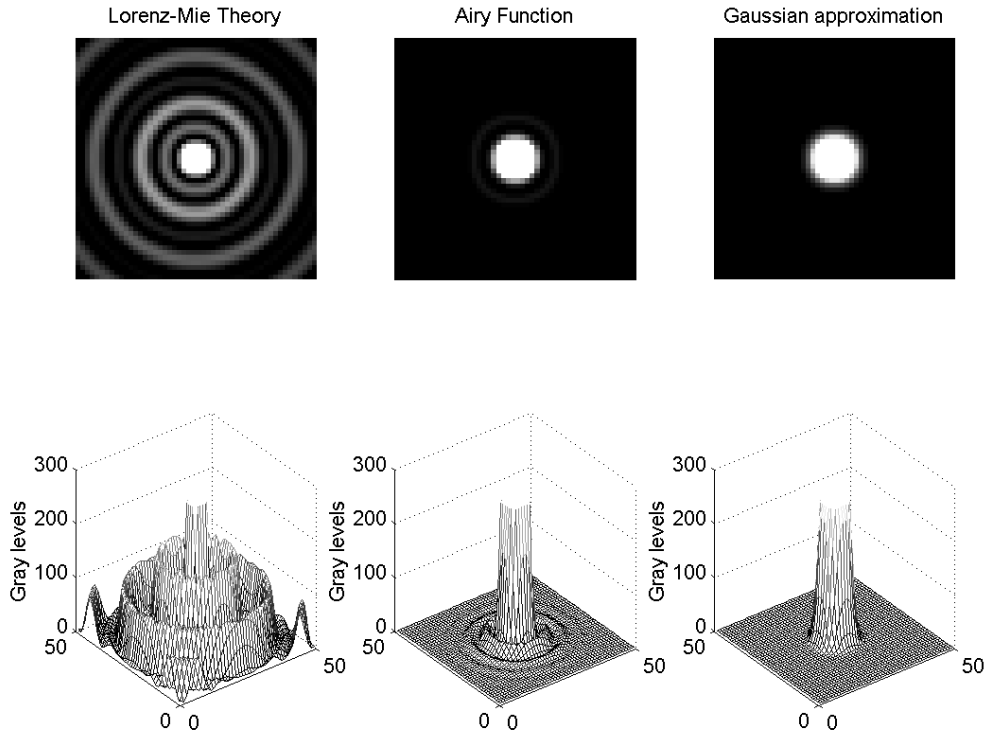


**Figure 5.3 Three different modelled calculations of a particle image, adjusted to 5 percent of its maximun intensity**

## 5.3 Experimental arrangement

The experimental set-up and experimental results compared to the calculations are fully described in [2], so they are briefly mentioned here to give an indication of the experimental conditions and results. For model verification purposes, calculations were made for a 50 μm particle at a laser wavelength λ = 337nm [3], and were found to be in close agreement with other authors' experimental/computational results, as well as results for a Gaussian wave-front.

The experimental set-up included provision for recording forward scattering, back

scattering, and the more conventional orthogonal viewing of a thin light-sheet for PIV. Particles were deposited on a microscope slide held by a x-y-z micrometer holder. The slide was anti reflection coated to optimize the signal-to-noise ratio. Three modes of illumination were investigated, a plane wave-front as they are normally considered by classical LMT, a Gaussian wave-front as normally employed in particle sizing applications, and a light sheet as in conventional PIV. Two lasers were used for these tests, a stable He-Ne and a frequency doubled Nd:YAG, for viewing small particles. A range of particle sizes was investigated. These ranged from water, to glass spheres and pollen. Actual particle sizes were verified by microscopic techniques. Available sizes ranged from 4 μm to 150 μm.

**5.4 Results and discussion**

The difference in intensity distribution exhibited by particles that are an equal distance out of focus but on opposite sides of the object plane of the lens, has been observed and reported previously [3,4]. It becomes more significant as particle size decreases, contributing to the accuracy of the 3D positioning model presented here, a feature that can be clearly seen in the calculations. Figure 5.4 shows a plot for the image of a 18 μm particle at a magnification of 7.85, for a range of defocus going from - 5.0 mm to + 5.0mm. Note that no size-related simplification is included in the model, and therefore the calculations are valid for micron-sized particles, as employed in unsteady flow research using velocimetry. Larger particles were used for convenience only.

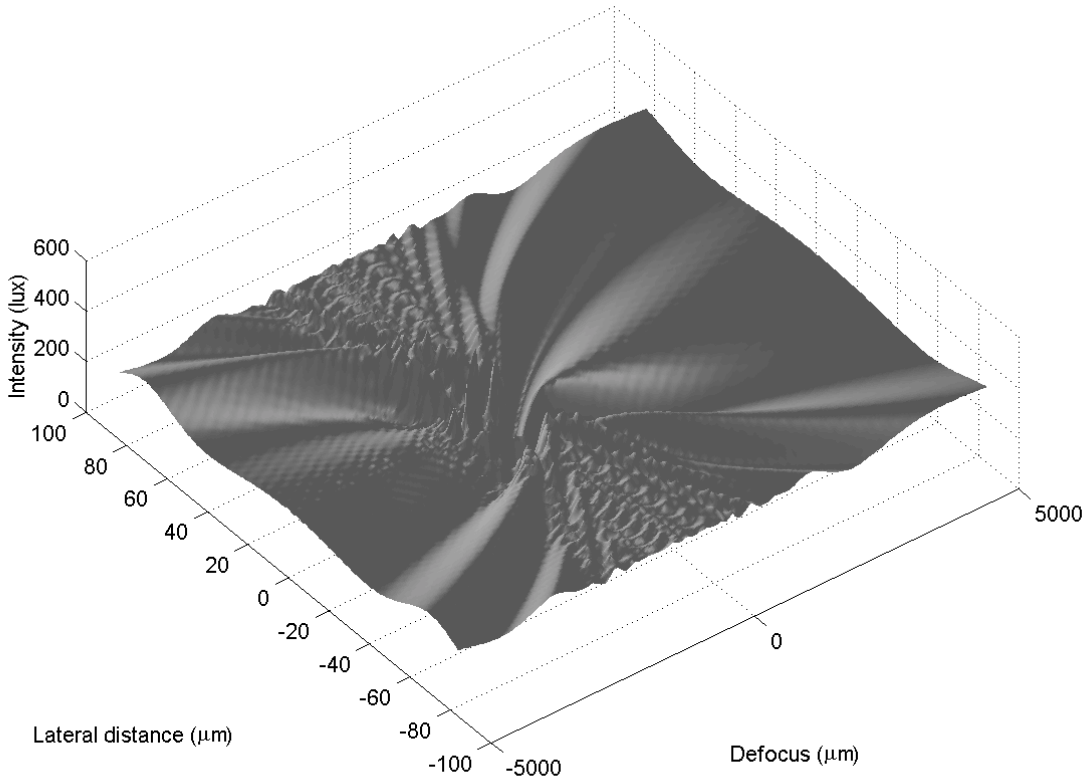


**Figure 5.4 Mesh plot of particle image vs. Defocus (Experimentally-verified gaussian-beam generalized Lorenz-Mie calculation – 18 μm glass particle).**

Using the GLMT allows to model the particle position accurately anywhere in the beam, using the three most commonly used wave-fronts: plane wave, Gaussian beams, and light sheets. This model has been verified against experimental data by the authors of this thesis, and to numerical calculations obtained by other authors [ ]. To illustrate this point see figure 5.5, where an experimental image intensity of a particle with diameter 18 μm is shown compared to the image intensity of the particle calculated using the GLMT toolbox (shown in figure 5.6) for forward scattering and Gaussian illumination, as in other

published data and calculations. The difference between the calculated and experimental image was 11 gray levels RMS, with a positional accuracy of 5 μm at a magnification of 7.85. The particle position accuracy has been estimated as 20 μm at low magnifications. For comparison, calculations using classical Lorenz-Mie Theory yielded positional accuracies of the order of 50 μm. The position accuracy can be improved by increasing magnification, at the cost of reducing the size of the investigation region. For high-speed unsteady flow research using velocimetry techniques, areas of interest are small but require magnifications in the range of 1x to 3x at most, using current CCD technology.

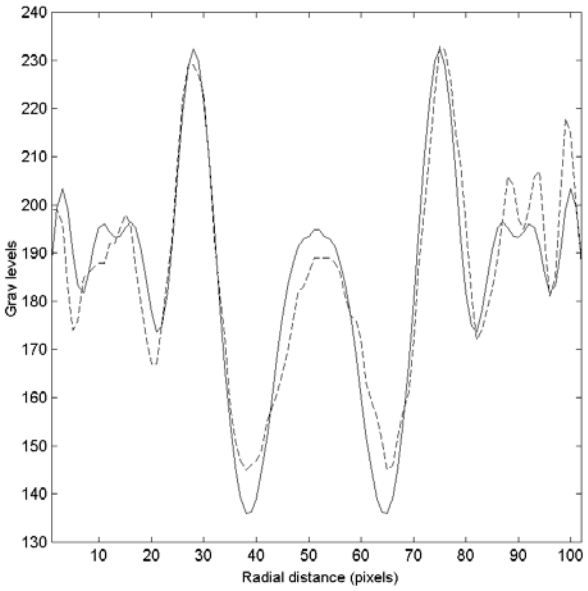


**Figure 5.5 Comparison of radial intensity for experimental (dashed) vs. theoretical (solid) particle images.**

Figure 5.6 shows the front-end of the GLMT toolbox code, written in MATLAB 5.3. Facilities are included for changing particle physical parameters as well as illumination source, lens parameters, wave-front parameters and orientation. Calculations can be

compared to experimental results and visualized using user-specified digitization parameters.

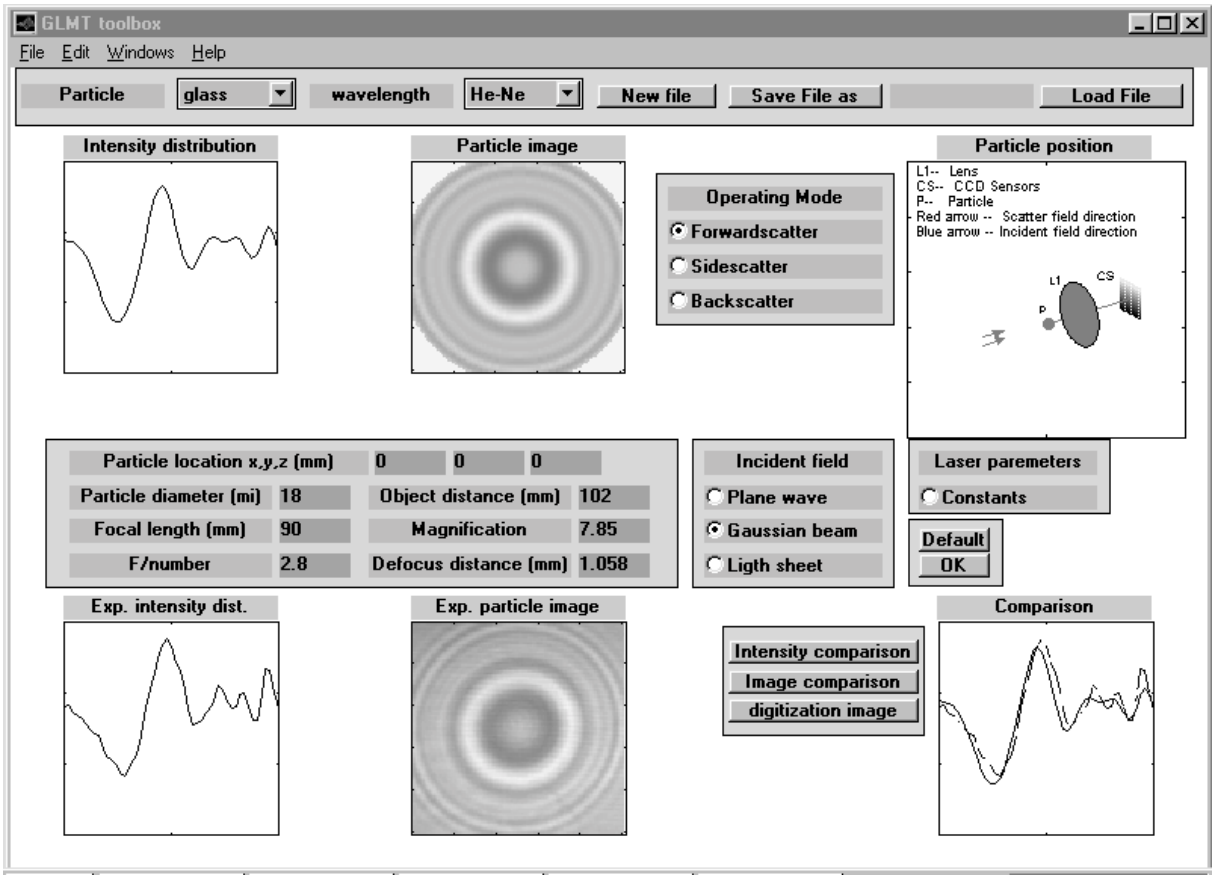


**Figure 5.6 Typical GLMT toolbox front-end display.**

## 5.5 Concluding remarks

The theoretical model described can also be easily extended to a more complex imaging system geometry involving multi-lens or fiber-optic systems, for instance, since it is well known that a multi-lens system can be approximated to a single lens with characteristics equal to the lens system. A code has been developed from the mathematical model which includes for the first time, not only the theoretical considerations of GLMT,

but also its practical implementation in order to obtain realistic particle images. Micrometer sized particle diffraction images have been quantitatively compared to experimental data for the first time to the best of my knowledge.

## References

1. Guerrero, A., Mendoza Santoyo, F., Funes-Gallanzi, M., "Particle positioning from CCD images: experiments and comparison to the Generalized Lorenz-Mie Theory", submitted to Measurement Science and Technology, (1999).

# Chapter 6
# Conclusions and future work

## 6.1 Conclusions

PIV is a whole-field method of measuring fluid velocity almost instantaneously. This approach combines the accuracy of single point methods with the multipoint nature of flow visualisation techniques.

PIV suffers from several major disadvantages. These include, among others, that the technique of dual-point optical access needed for orthogonal viewing a thin light sheet is intrinsically 2D. Alternative techniques for PIV three-dimensional investigation of fluid flow have been proposed, at the cost of increased complexity and optical access, and in some cases giving up a real-time measurement capability.

In an attempt to solve some of the above cited problems this thesis present the use of the GLMT and Fresnel approximation to the Huygens-Fresnel propagation theory for particle image calculation it is a novel contribution to three dimensional velocity measurements in these fields. Intensity and spatial information of a particle image diffraction pattern is used to calculate its three-dimensional position, and hence velocity information using real-time CCD cameras.

The Lorenz-Mie Theory (LMT) gives the general expressions for electromagnetic scattering by spherical, homogeneous and isotropic scatterers by using a waveplane illumination. The Generalized Lorenz-Mie Theory (GLMT) deals with a scattering theory for a spherical scatterer with arbitrary location in an arbitrary incident profile such as a laser beam or a ligth sheet. The electric field scattered by the spherical small particle is used to calculate image particle.

Propagation of the electric field through the imaging system components is developed from scalar viewpoint using the thin-lens transformation and the Fresnel approximation to the Huygens-Fresnel propagation equation. The model also include Seidel aberrations of the optical system used, such that accuracy of the model is improved, and thereby increasing the accuracy of the particle positioning algorithm. Although the theoretical model presented has been simplified extensively over the actual physical problem, the results agree qualatatively with experimental observations.

The theoretical model described can also be easily extended to a more complex imaging system geometry involving multi-lens or fiber-optic systems, for instance, since it is well known that a multi-lens system can be approximated to a single lens with characteristics equal to the lens system. A code has been developed from the mathematical model which includes for the first time, not only the theoretical considerations of GLMT, but also its practical implementation in order to obtain realistic particle images. Micrometer sized particle diffraction images have been quantitatively compared to experimental data for the first time to the best of my knowledge.

Another important task in PIV is the ability of to provide velocity data, obtained simultaneously, on a distributed spatial grid. This is of interest in using the data to validate CFD codes. Moreover is important to know how much detail can be obtained by sparse random 2D point measurements of a velocity field. This thesis also proposed a method to determine the optimum grid size for interpolated velocimetry data, without making any a-priori assumptions about the velocity fields, the system used or analysis method. The method employs condition number as the main criterion for deciding the adequate grid size

for a given data set. Data sets are directly comparable, independently of differing experimental parameters or data processing methods.

There are three sets of independent constraints in PIV measurements, which must be related. Firstly, the physical characteristics of the sensor with which the PIV image is to be recorded. Secondly, the range of scales in the velocity field under investigation (ranging from those of the same order as the characteristic length down to the Kolmogorov scale). Thirdly, once the data has been analysed and the velocity vectors calculated, the grid separation for an interpolated representation of the continuos field must be defined. The unifying concept for these three constraints is the condition number. The latter can be regarded as the ratio of the resolution to the largest sensor axis in the first case, the ratio of the characteristic length to the Kolmogorov scale in the second, and the sensitivity of the approximating matrix to perturbations in the third.

By setting the resolution to be equal to the Kolmogorov scale, the required sensor size and magnification are fixed and the first and second constraints are made consistent. The third constraint requires the determination of a grid separation which exhibits minimum error without detailed knowledge of the velocity field under investigation. This is achieved by setting the condition number of the interpolation to twice the condition number of the flow field. Finally, the calculated grid size requires the number of mesh points which need to be used to compare numerical calculations to experimental data.

### 6.2 Future work

Much work remains in refining the code, speeding it up, extending it so all forms of aberrations are considered, also taking into account various aperture shapes. However, having an accurate quantitative particle image model is an important step forward for

velocimetry applications. Being able to find 3D particle positioning from CCD camera images opens the way for routine accurate 3D-velocity estimation.

These concepts studied in the optimum velocimetry data display method are at an early state of application to PIV analysis, and much work remains to be done. However, an analytical description of all the parameters involved in PIV are thus beginning to be developed to enable the implementation of high-accuracy measurements in all conditions. This approach opens the way for the investigation of complex flows with high accuracy and detail at the cost of extra processing, though this is increasingly economically feasible and widely available.